UNIVERSITY OF CALIFORNIA,
IRVINE

Dispersive Real Time Laser Scanner and Scalability Approaches

THESIS

submitted in partial satisfaction of the requirements
for the degree of

MASTER OF SCIENCE

in Electrical Engineering

by

Rasul Torun

Thesis Committee:
Professor Ozdal Boyraz, Chair
Professor Ahmed Eltawil
Professor Filippo Capolino

2018

DEDICATION

To my family...

TABLE OF CONTENTS

LIST OF FIGURES

Page

LIST OF TABLES

ACKNOWLEDGMENTS

I would like to express my sincere gratitude to my advisor, Prof. Ozdal Boyraz, for his guidance, support and time. Also, I would like to thank my committee members, Prof. Ahmed Eltawil and Prof. Filippo Capolino for their time and suggestions.

Additionally, I would like to thank my senior labmate Salih Kalyoncu who helped me to improve my experimental skills and familiarize the field of optics. His advice and supervision was priceless to pursue research in this field. Also, I would like to thank my another senior labmate, Yuewang Huang who designed and fabricated the GPM-based blazed grating that is employed to improve the power efficiency of the system.

I would like to take this opportunity to also thank all my colleagues who have persistently cooperated with me and guided me in my research. In particular, I would like to extend my warmest appreciation to Salih Kalyoncu, Yuewang Huang, Qiancheng Zhao, Alan Tam, Shah Rahman and Tuva Atasever for their encouragement and support.

I gratefully acknowledge the research fellowship received from the Scientific and Technological Research Council of Turkey (TUBITAK) during my graduate studies.

To sum up, special thanks to my family for supporting and encouraging me all the time.

ABSTRACT OF THE THESIS

Dispersive Real Time Laser Scanner and Scalability Approaches

By

Rasul Torun

Master of Science in Electrical Engineering

University of California, Irvine, 2018

Professor Ozdal Boyraz, Chair

Dispersive Fourier Transform (DFT) is a measurement technique that facilitates wavelength to time mapping through optical dispersive elements with large and linear group velocity dispersion (GVD) such as dispersive fibers or chirped fiber bragg gratings (CFBG). This technique has been applied to several scientific and industrial applications such as analog to digital converters to increase effective sampling rates, spectroscopy to enable single-shot real-time spectral measurements, optical arbitrary waveform generation, and real time imaging to capture fast dynamic processes.

In this work, Dispersive Fourier Transformation and its application on real time imaging are investigated. We demonstrated a fast dispersive laser scanning system that can achieve horizontal scanning through Raman amplified DFT and diffraction grating system and vertical scanning by employing MEMS based digital micro mirror arrays technology. The proposed technique employs real time dispersive imaging system, which captures spectrally encoded images with a single photodetector at pulse repetition rate via space-to-time mapping technology. Wide area scanning capability is introduced by using individually addressable micro mirror arrays as a beam steering device.

Experimentally, we scanned $\sim$20mm^2 at scan rate of 5kHz with $\sim$150μm lateral and $\sim$160μm vertical resolution that can be controlled by using 1024x768 mirror arrays. With the current

state of the art MEMS technology, fast scanning up to 32.5kHz scan rate and resolution down to single mirror pitch size of 10.8μm is also achievable. Moreover, we investigated and demonstrated the ideas to improve the system to achieve larger area scan with faster scan rates and higher resolution while optimizing power.

Chapter 1

Introduction

The idea of time stretching, as a technique to slow down electrical signals, goes back to the mid 19^{th} century. It facilitates linear dispersive elements to manipulate the signal frequency. A novel all-electrical time-stretch system was first demonstrated by William Caputi [1]. The capability of the all-electrical system was limited, since the available dispersive elements in the electrical domain has small bandwidth. On the other hand, ultra-high bandwidth (up to THz) dispersive elements such as single mode fiber (SMF) [2], chirped fiber Bragg gratings (CFBG) [3], and prisms [4], are available in optical domain. Optical time stretch systems that utilize SMF as a dispersive medium, was demonstrated experimentally at the end of the century [5, 6].

The first application employing the technique was the Time Stretch Analog-to-Digital Converter (TS-ADC), since ADC is the key bottleneck in high performance communication systems due to rapid developments in digital signal processor (DSP) technology [7]. Thus, it is necessary to slow down the high frequency electrical signals operated by the DSPs prior to digitization, which could not exceed a few GSa/s sampling rates.

Additionally, time stretching is employed to utilize real-time applications such as optical

arbitrary waveform generation (AWG) [2] and optical imaging [8] via slowing down the pulse envelope that is spatially modulated. In such systems, the broadband super continuum (SC) source is followed by the dispersive components, where the broadening effect maps the time and wavelength components, namely time-wavelength mapping. The technique is also called Dispersive Fourier Transform (DFT) [9], since the time domain signal takes the shape of its spectrum at the end of dispersion compensation module (DCM).

This thesis is aimed to explain the DFT and its application on real time dispersive laser scanner. Chapter 1 is a general introduction to the thesis. In Chapter 2, background information that includes pulse propagation inside the dispersive fiber, lumped and distributed optical amplifiers and optical detection along with free-space components such as digital micro-mirrors as beam steering devices and diffraction gratings are delivered. Also, the simulation results obtained by Split Step Fourier Method (SSFM) on group velocity dispersion (GVD) and self phase modulation (SPM) are presented in this chapter. In Chapter 3, we proposed a wide-field real time imaging technique utilizing MEMS based digital micro mirror devices (DMDs) to observe surface characteristics in microfabrication, microfluidic flow for blood screening in medicine, etc. The working principle of the laser scanner system and its submodules are discussed in the chapter. By employing this scanner, we scanned $\sim$20 mm^2 wide area experimentally at a scan rate of 5 kHz with achieving $\sim$150μm lateral and $\sim$160μm vertical resolution via controlling 1024x768 mirror arrays. With the current state of art equipment, our system can reach fast scanning with less than 30μs and resolution down to single mirror pitch size of 10.8μm [8]. On the other hand, the proposed system can be scaled up in terms of speed, power and area. The speed and power scaling can be achieved via altering DMD and diffraction grating respectively with state of the art equivalents. Additionally, the scanned area can be increased with employing several DMDs in a parallel setup. Such concepts to improve system performance are presented in Chapter 4. Finally, Chapter 5 gives a brief conclusion to the thesis.

Chapter 2

Background

In this chapter, fundamentals of the background theory used in dispersive systems, especially in real-time dispersive laser scanner are presented. The laser scanner system consists of both fiber based and free space based subsystems. Fiber based subsystems are supercontinuum (SC) generation and dispersive fourier transform (DFT) that are facilitating nonlinear and linear properties of optical fibers respectively. Therefore, first, pulse propagation in fibers is explained in here. On the other hand, in free space, 2D scanning is achieved via digital micro mirror device (DMD) and diffraction grating. The diffraction grating provides lateral scanning through wavelength to space mapping. Therefore, 4-f lens system is built with a cylindrical lens to stop separation of different wavelengths in lateral dimension, but to generate exact 1-to-1 mapping of the individual wavelengths from the diffraction grating surface to the target and single pixel detector plane. Therefore, the theory of DMD, diffraction gratings and lens systems will be explained. Additionally, in order to achieve high signal to noise ratio (SNR) at the detector, both lumped and distributed amplification schemes are employed. Therefore, at the end, theory of optical amplification and detection is presented.

2.1 Pulse Propagation in Fibers

2.1.1 Nonlinear Schrödinger Equation

Both linear dispersive and nonlinear effects influence the propagating optical pulses inside a fiber. The linearity in optics is defined by intensity independence [10]; therefore fiber becomes nonlinear especially for intense short pulses ranging from ∼10ns to 10fs. Both nonlinear and the dispersive effects change the pulse shape and spectra. As it is well known, light is also an electromagnetic wave; therefore its propagation inside the fiber is governed by Maxwell's equations [11].

$$\nabla \times E = -\frac{\partial B}{\partial t} \tag{2.1a}$$

$$\nabla \times H = J + \frac{\partial D}{\partial t} \tag{2.1b}$$

$$\nabla \cdot D = \rho_f \tag{2.1c}$$

$$\nabla \cdot B = 0 \tag{2.1d}$$

where D (C/m^2) and B (Wb/m^2) are the electric and the magnetic flux densities that are related to corresponding electric and magnetic field vectors E (V/m) and H (A/m) through equations:

$$D = \varepsilon_0 E + P \tag{2.2a}$$

$$B = \mu_0 H + M \tag{2.2b}$$

where ε_0 (F/m) is the electric permittivity and μ_0 (H/m) is the vacuum permeability which are related to speed of light via the equation c=$\frac{1}{\sqrt{\varepsilon_0 \mu_0}}$ (m/s). P (C/m^2) and M (Wb/m^2) are the induced electric and magnetic polarization vectors, respectively. When we consider the optical fiber, the equations are further simplified because of the non-magnetic medium

($M = 0$), and the absence of free charges (ρ_f=0) and free current ($J = 0$). The wave equation that describes the propagation of light inside the fiber can be obtained by substituting Eq. (2.2) into Maxwell's equations and taking the curl of Eq. (2.1a), that leads to:

$$\nabla^2 E(r,t) - \frac{1}{c^2}\frac{\partial^2 E(r,t)}{\partial t^2} = \mu_0 \frac{\partial^2 [P_L(r,t) + P_{NL}(r,t)]}{\partial t^2} \tag{2.3}$$

where P_L and P_{NL} are the linear and the nonlinear components of the induced electric polarization defined as:

$$P_L(r,t) = \varepsilon_0 \int_{-\infty}^{\infty} \chi^{(1)}(t - t^{'}) E(r,t^{'}) dt^{'} \tag{2.4}$$

$$P_{NL}(r,t) = \varepsilon_0 \left[\int_{-\infty}^{\infty} \int_{-\infty}^{\infty} \chi^{(2)}(t - t^{'}) E^2(r,t^{'}) dt^{'} dt^{'} \right] + \varepsilon_0 \left[\int_{-\infty}^{\infty} \int_{-\infty}^{\infty} \int_{-\infty}^{\infty} \chi^{(3)}(t - t^{'}) E^3(r,t^{'}) dt^{'} dt^{'} dt^{'} + \ldots \right] \tag{2.5}$$

where $\chi^{(n)}$ is the n^{th} order susceptibility of the dielectric medium. In Eq.(2.5), 2^{nd} order term vanishes due to inversion symmetry of silica fibers and the third order susceptibility $\chi^{(3)}$ becomes dominant that creates main nonlinear effects such as SPM and Raman scattering [11]. Thus, P_L and P_{NL} are approximated as:

$$P_L = \varepsilon_0 \chi^{(1)} E(r,t) \tag{2.6a}$$

$$P_{NL} \approx \varepsilon_0 \varepsilon_{NL} E(r,t) \tag{2.6b}$$

where

$$\varepsilon_{NL} = \frac{3}{4}\chi^{(3)} |E(r,t)|^2 \tag{2.6c}$$

The following assumptions are made in order to solve the wave equation in Eq.(2.3) [11]:

i The induced nonlinear polarization (P_{NL}) is so weak (causes less than 10^{-6} refractive index change), hence treated as a small perturbation.

ii The polarization is preserved along the fiber.

iii Slowly varying envelope approximation is used, because the field is quasi-monochromatic ($\Delta\omega/\omega_0 \ll 1$), where $\Delta\omega$ (Hz) is the bandwidth of the field and ω_0 (Hz) is the central frequency.

The propagation equation Eq.(2.3) fits better in the Fourier domain after simplifications and transforms to:

$$\nabla^2 E(r,\omega) + \varepsilon(\omega) k_0^2 E(r,\omega) = 0 \tag{2.7}$$

where the complex permittivity $\varepsilon(\omega) = \varepsilon_0(1 + \tilde{\chi}^{(1)}(\omega) + \tilde{\chi}^{(3)}(\omega) + \tilde{\chi}^{(5)}(\omega) + \ldots)$, $\tilde{\chi}^{(n)}$ is the Fourier transform of $\chi^{(n)}$ and the wavenumber $k_0 = \omega_0/c$ (rad/m). The refractive index (n) and the absorption coefficient (α) can be derived from the dielectric constant via

$$\varepsilon = \left(n + i\frac{\alpha}{2k_0}\right)^2 = (n_L + \Delta n)^2 \tag{2.8}$$

Therefore, they consist of both linear and nonlinear terms described by

$$n = n_L + n_{NL} = n_L + n_2|E|^2 \tag{2.9a}$$

$$\alpha = \alpha_L + \alpha_{NL} = \alpha_L + \alpha_2|E|^2 \tag{2.9b}$$

where the nonlinear index coefficient $n_2 = \frac{3}{8n}\Re\left[\chi^{(3)}\right]$ and two-photon absorption coefficient $\alpha_2 = \frac{3\omega_0}{4nc}\Im\left[\chi^{(3)}\right]$. The dielectric constant is mainly calculated by the refractive index and the absorption loss is added as a small perturbation as mentioned in the equation Eq. (2.8) where $\Delta n = n_2|E|^2 + i\frac{\alpha}{2k_0}$.

The separation of variables method can be used to solve Helmholtz Equation in Fourier domain and the solution will be in the form of:

$$E(r,\omega) = F(x,y)A(z,\omega)exp(i\beta_0 z) \tag{2.10}$$

where $F(x,y)$ is the field distribution of the fiber mode, $A(z,\omega)$ is the slowly varying envelope and the β_0 is the wave number. The mode distribution and the envelope equations can be derived from Eq.(2.7), when $E(r,\omega)$ terms replaced by the Eq.(2.10).

$$\frac{\partial^2 F(x,y)}{\partial x^2} + \frac{\partial^2 F(x,y)}{\partial y^2} + (\beta_0^2 - \bar{\beta}^2)F = 0 \tag{2.11}$$

$$2i\beta_0 \frac{\partial A}{\partial z} + (\bar{\beta}^2 - \beta_0^2)A = 0 \tag{2.12}$$

The first equation is solved by treating Δn as a first order perturbation, hence $\varepsilon = (n_L + \Delta n)^2 \approx n_L^2$. Therefore, $F(x,y)$ is independent of the nonlinear perturbation (Δn). The wave number is also defined as the sum of the linear and nonlinear terms respectively as in $\bar{\beta}(\omega) = \beta(\omega) + \Delta\beta(\omega)$.

$$\Delta\beta(\omega) = \frac{\omega^2 n(\omega)}{c\bar{\beta}(\omega)} \frac{\int_{-\infty}^{\infty}\int_{-\infty}^{\infty} \Delta n(\omega)|F(x,y)|^2 dxdy}{\int_{-\infty}^{\infty}\int_{-\infty}^{\infty} |F(x,y)|^2 dxdy} = i\frac{\alpha}{2} + \gamma|A|^2 \tag{2.13}$$

where $\gamma = \frac{n_2\omega_0}{cA_{eff}}$ is the nonlinear parameter and $A_{eff} = \frac{\left[\int_{-\infty}^{\infty}\int_{-\infty}^{\infty} |F(x,y)|^2 dxdy\right]^2}{\int_{-\infty}^{\infty}\int_{-\infty}^{\infty} |F(x,y)|^4 dxdy}$ is the effective mode area. The linear and nonlinear wave number terms are expanded by using Taylor

expansion around the carrier frequency ω_0, as shown below.

$$\beta(\omega) = \beta_0 + \sum_{j=1}^{\infty} \frac{1}{j!}\beta_j(\omega - \omega_0)^j \tag{2.14a}$$

$$\Delta\beta(\omega) \approx \Delta\beta_0 \tag{2.14b}$$

$$\bar{\beta}(\omega) \approx \beta_0 + \sum_{j=1}^{\infty} \frac{1}{j!}\beta_j(\omega - \omega_0)^j + \Delta\beta_0 \tag{2.14c}$$

where β_j is the jth order linear dispersive term and $\Delta\beta_0$ is the zeroth order nonlinear term.

By using the approximation $(\bar{\beta}^2 - \beta_0^2) \approx 2\beta_0\left[\bar{\beta}(\omega) - \beta_0\right]$ and substituting $\bar{\beta}(\omega)$ with Eq.(2.14c), Eq.(2.12) simplifies to [12]

$$\frac{\partial A}{\partial z} - i\sum_{j=1}^{\infty} \frac{1}{j!}\beta_j(\omega - \omega_0)^j A = i\Delta\beta_0 A \tag{2.15}$$

Further by substituting $\Delta\beta_0$ with $i\frac{\alpha}{2} + \gamma|A|^2$ and taking the inverse Fourier transform of both sides of Eq. (2.15), the well known Nonlinear Schrödinger Equation (NLSE) for A(z,t) is derived as:

$$\frac{\partial A}{\partial z} + \sum_{j=1}^{\infty} \frac{-i^{j+1}}{j!}\beta_j \frac{\partial^j A}{\partial t^j} = -\frac{\alpha}{2}A + i\gamma(\omega_0)|A|^2 A \tag{2.16}$$

The NLSE simplifies to

$$\frac{\partial A}{\partial z} + \beta_1\frac{\partial A}{\partial t} + i\frac{1}{2}\beta_2\frac{\partial^2 A}{\partial t^2} - \frac{1}{6}\beta_3\frac{\partial^3 A}{\partial t^3} + \frac{\alpha}{2}A = i\gamma|A|^2 A \tag{2.17}$$

after neglecting the higher order dispersion ($\beta_j = 0, j > 3$).

The simplified NLS equation (Eq. (2.17)) includes the effects of group velocity, group velocity dispersion, GVD slope, fiber loss, and fiber non-linearity respectively. The β_1 (s/m) is the reciprocal of group velocity and the β_2 (ps^2/km) is the GVD parameter of the propagation

medium. GVD slope (β_3) is negligibly small, unless second order dispersion is $\sim$0 [11].

2.1.2 Group Velocity Dispersion

Group velocity is defined as the effective velocity of a wave packet that includes several frequency components. In an optical dispersive medium, the lights with different colors (frequencies) travel at different velocity. Since speed is associated with the refractive index, dispersion means having different refractive indices for different colors. In bulk materials dispersion is a material property. In fibers, the net dispersion has two parts: material and waveguide dispersion that are originated from the nature of the material used to propagate light and the optical waveguide design such as its geometry and materials used in core and cladding parts. In an optical fiber, phase velocity can be defined as $\nu_g = c/n(\omega)$ in terms of frequency. Generally, there are two types of dispersion such as normal and anomalous. In normal dispersion, the lower frequencies (red shifted) travel faster than higher frequencies (blue shifted) and it is vice versa for anomalous dispersion. The optical wave starts to broaden because of the speed difference between different frequency components. The effect of GVD on the pulse propagation in a linear medium can be studied by eliminating all the nonlinear terms in Schrdinger equation, which results to a simplified NLSE:

$$i\frac{\partial A}{\partial z} = -\frac{\beta_2}{2}\frac{\partial^2 A}{\partial t^2} \tag{2.18}$$

This simplified differential equation can easily be solved by Fourier transform method. The normalized, arbitrary shaped pulse in time domain $A(z,t)$ and its spectrum $\hat{A}(z,\omega)$ in frequency domain are related by Fourier transform as:

$$A(z,t) = \frac{1}{2\pi}\int_{-\infty}^{\infty} \hat{A}(z,\omega)\exp(-i\omega t)d\omega \tag{2.19}$$

By taking the Fourier transform of both sides in Eq. (2.18) with using time derivative property $\left(\frac{\partial^n}{\partial t^n} \rightarrow (i\omega)^n\right)$, it transforms into an ordinary differential equation:

$$i\frac{\partial \hat{A}}{\partial z} = -\frac{1}{2}\beta_2\omega^2\hat{A} \tag{2.20}$$

which has a solution in the form of:

$$\hat{A}(z,\omega) = \hat{A}(0,\omega)\exp\left(\frac{i}{2}\beta_2\omega^2 z\right) \tag{2.21}$$

It is obvious from the solution that GVD alters only the phase, not the amplitude of the initial pulse spectrum. The added phase is proportional to the frequency and propagation length. The phase change in spectrum modifies the pulse shape in time domain as shown in Fig. 2.1. The corresponding time domain solution is evaluated by taking the inverse Fourier Transform of Eq. (2.21).

$$A(z,t) = \frac{1}{2\pi}\int_{-\infty}^{\infty}\hat{A}(0,\omega)\exp\left(\frac{i}{2}\beta_2\omega^2 z\right)\exp(i\omega t)d\omega \tag{2.22}$$

The femtosecond laser pulses used in optics do not have a well-defined shape due to nonlinear processes inside the laser cavity, distortions, and noise interference etc. However, they can be approximated as Gaussian pulses, which are well defined mathematically, in order to investigate the effect of optical system on the pulse. The following part is the review on the effect of GVD on the Gaussian pulses. A normalized Gaussian pulse defines the initial pulse:

$$A(0,t) = \exp\left[\frac{1+iC}{2}\left(\frac{t}{T_0}\right)^2\right] \tag{2.23}$$

where C is the initial chirp parameter and T_0 is the half width at $1/e$ intensity point and related to full width at half maximum as $T_{FWHM} = 1.665T_0$. The final pulse after propagation

becomes:

$$A(z,t) = \frac{T_0}{\sqrt{T_0^2 - i\beta_2 z(1+iC)}} \exp\left[-\frac{(1+iC)t^2}{2(T_0^2 - i\beta_2 z(1+iC))}\right] \tag{2.24}$$

The result shows that both initially chirped ($C \neq 0$) and unchirped ($C = 0$) Gaussian pulses conserve their Gaussian shapes after propagation. However, the pulse width T_1 (defined similar to T_0) and the chirp parameter C_1 of the pulse change due to GVD as [13]:

$$\frac{T_1}{T_0} = \left[1 + \left(\frac{C\beta_2 z}{T_0^2}\right)^2 + \left(\frac{\beta_2 z}{T_0^2}\right)^2\right]^{1/2} \tag{2.25}$$

$$C_1(z) = C + (1+C^2)\frac{\beta_2 z}{T_0^2} \tag{2.26}$$

According to the results, it is easily seen that, if there is no initial chirp on the pulse, the pulse starts to broaden due to GVD independent of the medium type such as normal ($\beta_2 > 0$) or anomalous ($\beta_2 < 0$). If there is an initial chirp, pulse broadens faster than unchirped case when $\beta_2 C > 0$. On the other hand, if $\beta_2 C < 0$, the pulse first compress to compensate the effect of initial chirp and then starts to broaden again [13].

Simulation Results

The following simulation results show the GVD effect on the Gaussian pulse in time and frequency domain. The results are obtained by using SSFM with zero nonlinearity.

Figure 2.1 and 2.2 show the evolution of transform limited and chirped Gaussian pulses along the fiber under the effect of GVD respectively. In the figures, the propagating pulses are displayed only at specific distances that are multiples of dispersion length, $L_D = \frac{T_0^2}{|\beta_2|}$, to

indicate the broadening and compression effects. Additionally, such pulses are normalized according to the peak intensity of the initial pulse. It is clearly seen in Fig. 2.1 that the GVD does not affect the spectrum intensity. However, time domain pulses are broadened due to phase change in the frequency domain. On the other hand, Fig. 2.2 demonstrates initially chirped pulse propagation where compression and faster broadening properties are observed. In addition to these, it is seen that Gaussian pulses remain Gaussian after propagation in linear dispersive mediums.

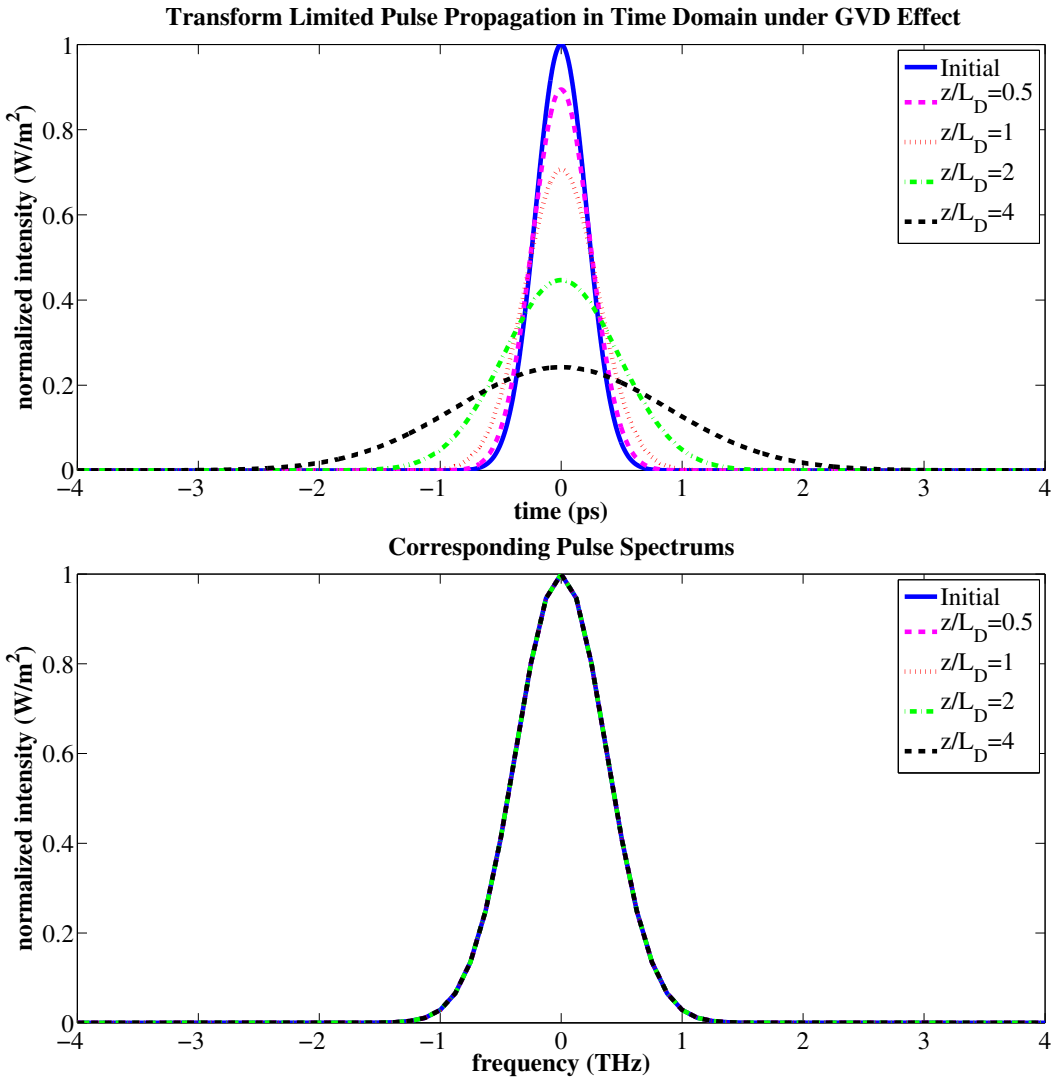

Figure 2.1: Transform limited Gaussian pulse ($T_{FWHM} = 500fs$) propagation inside a fiber. Temporal (upper) and Spectral (down) evolution due to GVD (D=17 ps/km-nm).

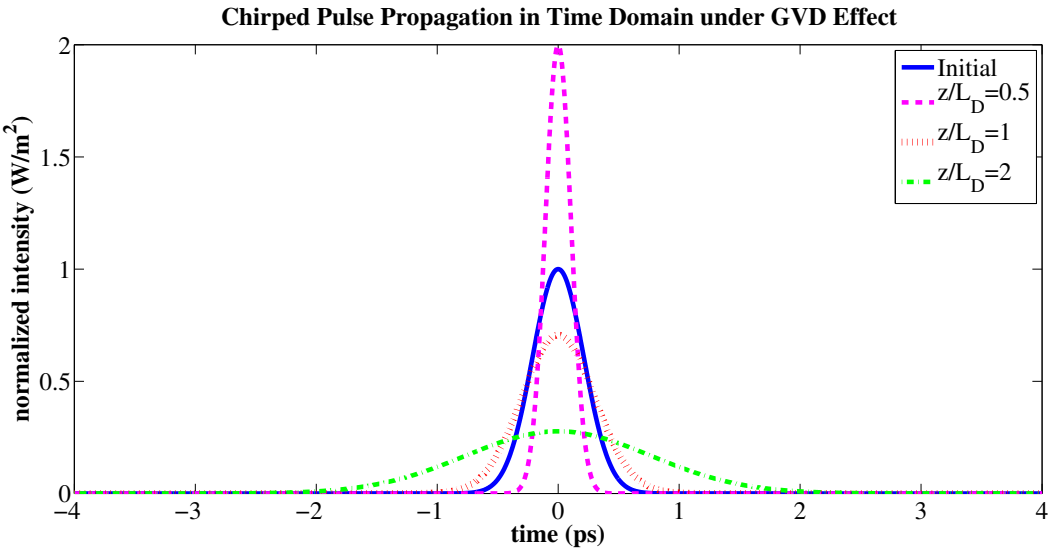

Figure 2.2: Chirped Gaussian pulse ($C = 2$) propagation inside a fiber under the effect of GVD (β_2=-21.67 ps^2/km). $L_D = \frac{T_0^2}{|\beta_2|}$ is the dispersion length.

2.1.3 Nonlinear Optical Effects

The optical medium becomes nonlinear, when the electromagnetic field (light) intensity increases due to small core area of the fiber and high peak power of the ultra short pulses. Self and Cross Phase Modulation (SPM/XPM) are two fundamental nonlinear effects.

Self Phase Modulation

Refractive index of the dielectric medium also depends on the intensity of the light, in addition to the frequency as in GVD. The refractive index profile becomes nonlinear, when the light intensity inside the medium increases. As a result, the pulse experiences both linear GVD and nonlinear effects while propagating in fiber. The comparison between the

dispersion and nonlinear length determines the dominant effect.

$$L_D = \frac{T_0^2}{|\beta_2|} \tag{2.27a}$$

$$L_{NL} = \frac{1}{\gamma P_0} \tag{2.27b}$$

where L_D, L_{NL} are dispersion and nonlinear lengths respectively, γ is the nonlinearity parameter and P_0 is the peak power of the pulse [11]. Three possible cases are shown below.

i) If $L > L_D$ and $L > L_{NL}$, both GVD and SPM is effective.

ii) If $L_D \gg L > L_{NL}$, then GVD is negligible.

iii) If $L_{NL} \gg L > L_D$, then SPM is negligible.

Therefore, the individual effect of SPM can be studied by eliminating GVD in NLS Equation (case 2). The equation simplifies to

$$\frac{\partial A}{\partial z} = ie^{-\alpha z}\gamma P_0 |A|^2 A \tag{2.28}$$

As it is seen in Eq. (2.28), SPM creates an intensity dependent nonlinear phase on the pulse without changing the pulse shape in time domain. However, the added phases would distort the spectrum drastically. The solution to the above ordinary differential equation is

$$A(z = L, t) = A(0, t) \exp[i\phi_{NL}(z = L, t)] \tag{2.29}$$

where $\phi_{NL}(L, t) = |A(0, t)|^2 \gamma P_0 L_{eff}$ is the nonlinear phase and $L_{eff} = \frac{1-\exp(-\alpha L)}{\alpha}$ is the effective length. The maximum phase shift occurs at the peak intensity point (center for the Gaussian pulses) and given by $\phi_{max} = \gamma P_0 L_{eff}$.

Any time dependent phase on the signal creates new frequency components in the spectrum as it is stated in Fourier Theorem. In other words, phase change across the pulse creates an instantaneous frequency deviation from the center value ω_0 that causes a spectral broadening. The amount of SPM induced spectral shift, also called frequency chirp ($\delta\omega$) is obtained by taking the derivative of nonlinear phase.

$$\delta\omega(t) = -\frac{\partial\phi_{NL}}{\partial t} = -\gamma P_0 L_{eff}\frac{\partial}{\partial t}|A(0,t)|^2 \tag{2.30}$$

For Gaussian pulses as in Eq. (2.23), the SPM induced frequency shift is:

$$\delta\omega(t) = -\frac{2}{T_0^2}\frac{L_{eff}}{L_{NL}}t\exp\left(-\frac{t^2}{T_0^2}\right) \tag{2.31}$$

with a maximum shift of $\delta\omega_{max} = 0.86\Delta\omega_0\phi_{max}$ where $\Delta\omega_0 = T_0^{-1}$.

Simulation Results

The effect of Self Phase Modulation both in time and frequency domains is shown in the following simulation results. The input pulse is again taken as the normalized Gaussian pulse. We can see that the spectrum is drastically distorted, while the pulse shape is conserved through the propagation, as mentioned before. The results are obtained by using SSFM with changing parameters to satisfy case 2 ($L_D \gg L > L_{NL}$).

The SPM makes spectral change, while preserving the time domain signals as opposed to GVD. As it is shown in Fig. 2.3, the SPM is nonlinear and it transforms the spectrum arbitrarily.

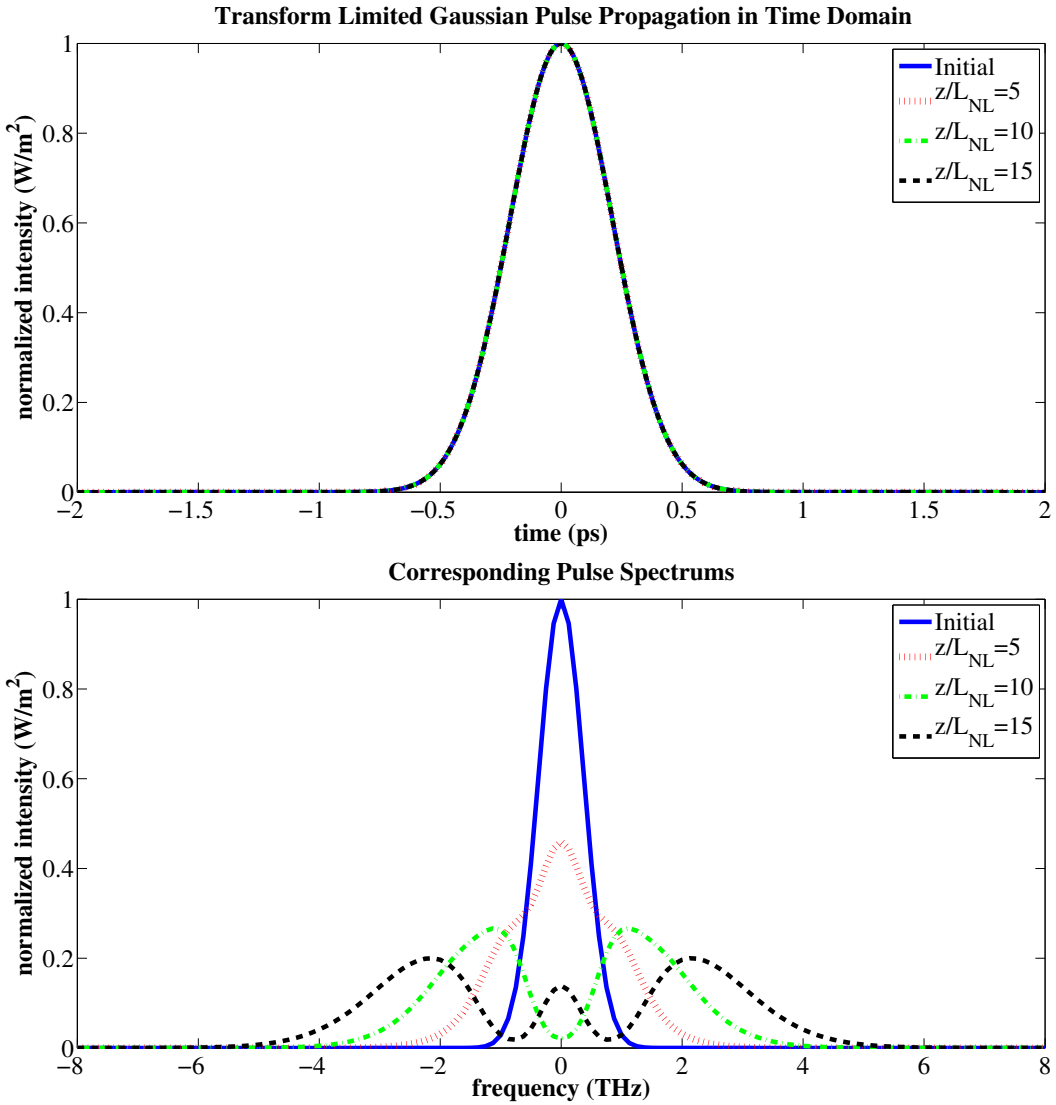

Figure 2.3: Transform limited Gaussian pulse propagation inside the fiber. Temporal (upper) and spectral (down) evolution due to nonlinear effect ($\gamma = 2W^{-1}km^{-1}$).

Cross Phase Modulation

Cross Phase Modulation is another nonlinear phenomenon similar to SPM, occurs when there are more than one optical beam in the medium at the same time. When the beams interact with each other, each optical beam experiences a refractive index change affected by its own intensity and the intensity of other beams that causes spectral broadening of the pulses [11]. The nonlinear phase caused by XPM is twice as high as SPM for the same intensity. As a result, the total nonlinear phase seen by each pulse due to SPM and XPM when N optical pulses with different frequencies propagate in a medium becomes [13]:

$$\varphi_j(t) = \gamma_j \left[L|A_j(0,t)|^2 + 2\sum_{j\neq k} \int_0^L |A_k(0, t - zd)|^2 dz \right] \tag{2.32}$$

where $j = 1 - N$. As seen in the above equation, XPM is also dependent to the relative positions of the pulses $(t - zd)$. The pulses only overlap in a certain time window, because they travel at different velocities in a dispersive medium. The walk-off between the pulses affects the amount of the spectral broadening due to XPM [14].

2.1.4 Numerical solutions to Nonlinear Schrödinger Equation

The full wave Maxwell equation does not generally have any analytical solution in nonlinear optical medium. Additionally, numerical solutions are very hard to apply due to dimensionality problem. However, an approximate solution can be found by using some predefined conditions and assumptions. There are simply two kinds of numerical methods such as pseudo spectral and finite difference methods that differ in terms of putting the carrier frequency into the account or not. The finite difference methods include the carrier frequency,

they can calculate forward and backward propagating waves more accurately than pseudo-spectral methods [15]. Split Step Fourier Method is one of the pseudo-spectral numerical methods that is extensively used to solve NLS equation for the propagation of pulses because of its easy implementation and fast computation [11]. In this study, I utilized SSFM method to investigate the pulse propagation inside the fiber.

Split Step Fourier Method

The fundamental idea of the SSFM is that the linear and nonlinear parts of NLS equation are treated separately using the analytical solutions of individual parts. Even though NLSE does not have any analytical solution, the individual linear and nonlinear parts have. They can be solved separately with a small numerical error by dividing the propagation distance into small steps (h). As a summary, the linear term due to GVD and nonlinear term due to SPM are defined respectively as [15]:

$$D = -\frac{\alpha}{2} - \sum_{m=2}^{3} \frac{i^{m-1}}{m!}\beta_m \frac{\partial^m}{\partial T^m} \tag{2.33a}$$

$$N = i\gamma \left[|A(z,t)|^2 + \frac{i}{\omega_0 A(z,t)} \frac{\partial}{\partial t}[|A(z,t)|^2 A(z,t)] \right] \tag{2.33b}$$

where $A(z,t)$ is the complex field envelope at distance (z) and time (t). Thus the NLS equation can be written in the form as [15, 16]:

$$\frac{\partial A(z,t)}{\partial z} = (D+N)A(z,t) \tag{2.34}$$

with a general solution of

$$A(z+h,t) = \exp[h(D+N)]A(z,t) \tag{2.35}$$

The solution is approximated by adding the dispersive and nonlinear effects independently over small distance (h) which is divided into two.

$$\exp[h(D+N)] = \exp(hD)\exp(hN) \tag{2.36}$$

The dispersion (D) effect is analyzed in frequency domain, since multiplication is computationally less complex than taking derivative in time domain. Thus, taking the Fourier Transform of both sides by using differentiation theorem, so NLS equation reduces to [15, 16]:

$$\frac{\partial A(z,\omega)}{\partial z} = -\frac{\alpha}{2}A(z,\omega) - \sum_{m=2}^{3}\frac{i^{m-1}}{m!}\beta_m(i\omega)^m A(z,\omega) \tag{2.37}$$

with the solution of

$$A(z+h,\omega) = A(z,\omega)\exp\left\{h\left[-\frac{\alpha}{2} - \sum_{m=2}^{3}\frac{i^{m-1}}{m!}\beta_m(i\omega)^m\right]\right\} \tag{2.38a}$$

$$A(z+h,t) = \mathcal{F}^{-1}\left\{A(z+h,\omega)\right\} \tag{2.38b}$$

In order to reduce the error accumulation more, we employed a modified technique called symmetrized SSFM in our simulations. The general procedure applied in symmetrized SSFM at every h distance is shown step by step below [15, 16]:

i) Dispersion and loss is calculated over h/2 by setting N=0.

$$A\left(z+\frac{h}{2},T\right) = \mathcal{F}^{-1}\left\{\exp\left[\frac{h}{2}D(i\omega)\right]\mathcal{F}\left\{A(z,T)\right\}\right\}$$

ii) At the midpoint of step size, nonlinearity is calculated by setting D=0.

$$A\left(z+\frac{h}{2},T\right)=A\left(z+\frac{h}{2},T\right)\exp(hN)$$

iii) Dispersion and loss is calculated over the second half by setting N=0.

$$A\left(z+h,T\right)=\mathcal{F}^{-1}\left\{\exp\left[\frac{h}{2}D(i\omega)\right]\mathcal{F}\left\{A(z+\frac{h}{2},T)\right\}\right\}$$

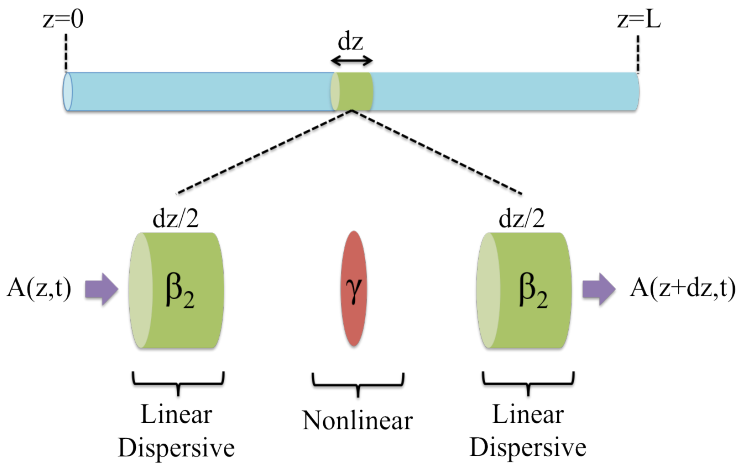

Figure 2.4: Schematic of Split Step Fourier Method [16].

2.2 Optical Amplification

In fiber optic systems, light intensity is degrading while propagating inside the optical fiber due to material absorption. Fig. 2.5 shows the loss spectrum of Corning SMF-28 single mode optical fiber. In long-haul fiber communication systems, 1550nm wavelength is employed due to minimum loss of 0.19 dB/km [17]. Before the invention of optical amplifiers in 1990s, optoelectronic repeaters or regenerators were utilized to overcome the loss and extend the reach of optical communications links. Such regenerators first convert the optical signal to electric current and then regenerate it via transmitter after amplification and processing to

clean the signal in electric domain. Even though, optical amplifiers do not able to regenerate the signal, they overcome the losses which are generally the main limiting factors. Also, they provide simultaneous amplification of wide-band optical signals through stimulated emission.

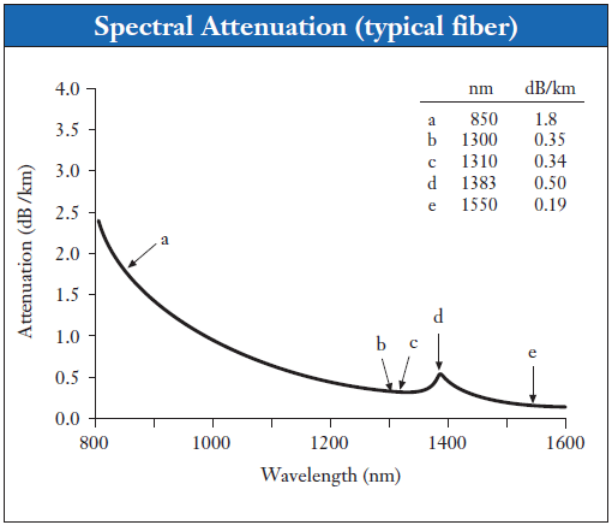

Figure 2.5: Spectral Attenuation of Corning SMF-28 single mode fiber [17].

Optical amplifiers can be categorized by the placement of gain medium as discrete and distributed amplification schemes. In discrete amplification scheme, the lumped amplifiers are placed at discrete positions, i.e. once in 40-60 km for modern fiber-optic communication systems. On the other hand, in distributed amplification, the entire fiber optic cable link used to propagate signal, is utilized as a gain medium with co-propagating and counter-propagating pumping schemes. Stimulated emission and stimulated Raman Scattering are the physical processes facilitated in these amplification schemes.

2.2.1 Discrete Amplification

The optical amplifiers used in discrete amplification are generally bulky optical devices, which require specially doped fibers to achieve desired gain profile. Erbium Doped Fiber Amplifier (EDFA) is the most commonly used discrete amplifier where the core of a silica fiber is doped with Erbium ions. In order to attain gain in communication wavelength (1550

nm), it needs to be efficiently pumped with a laser at a wavelength of 980 nm or 1450 nm [18]. EDFA has a narrowband gain curve and the pump wavelengths are determined by the resonant energy levels of Er atom, as shown in Fig. 2.6. Additionally, EDFA has a slow gain process because of the energy storage at the upper level of Er atom.

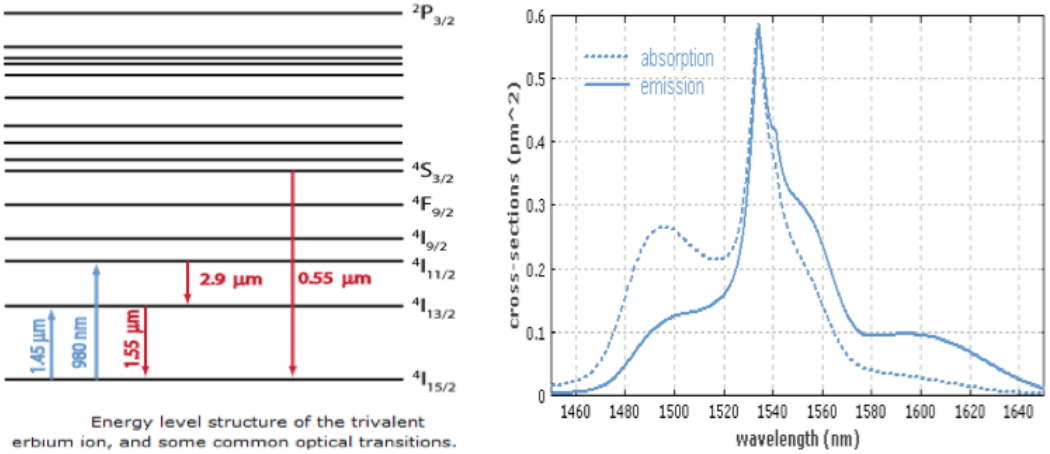

Figure 2.6: Energy level structure of Erbium ion and some optical transitions (a). Absorption and emission cross-sections for Erbium ions in Er: Yb-doped phosphate glass (b) [18].

2.2.2 Stimulated Raman Scattering

In molecular mediums, there is another nonlinear process called Stimulated Raman Scattering that is widely employed in optics to operate optical fibers as an amplifier or tunable laser by transferring energy from one beam (pump) to others (Stokes) [19]. In other words, the weak Stokes wave that has lower frequency ($E = h\nu$), thus higher wavelength ($\lambda = \upsilon_p/f$), is amplified by the intense (higher frequency) pump beam via SRS process. The vibrational energy states in the medium, as shown in Fig 2.7, determines the amount of energy transfer between incident and scattered fields.

The pump wave begins to amplify Stokes wave due to Raman induced energy transfer; when both the pump and probe (Stokes) waves simultaneously propagate inside a fiber. This

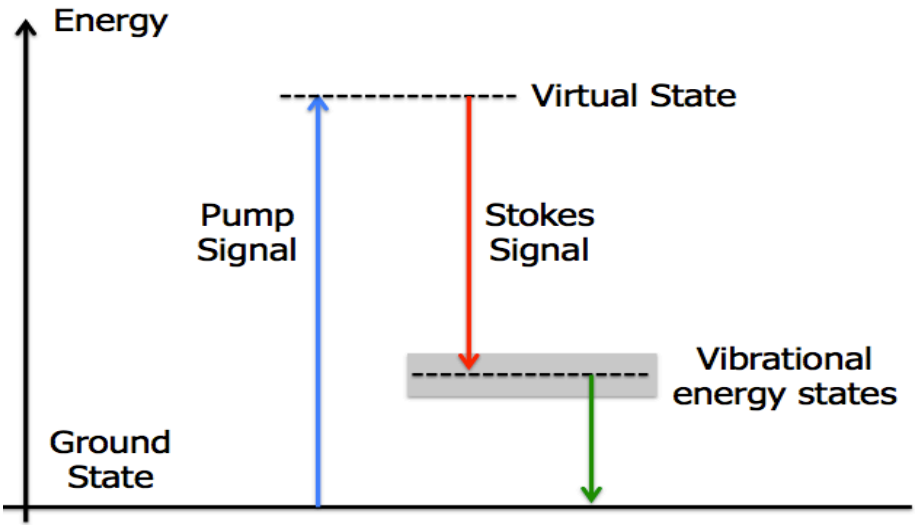

Figure 2.7: Energy Diagram of Raman Scattering [20].

amplification process is governed by the following equation in a lossless medium:

$$\frac{\partial I_S}{\partial z} = g_R I_P I_S \tag{2.39}$$

where I_S and I_P are Stokes and pump waves respectively and g_R is the Raman gain coefficient [21], which is a function of frequency shift ($\Omega = \omega_P - \omega_S$) between the pump and Stokes waves, and depends on the composition of the fiber core, relative polarization of both fields (co-polarized or orthogonally polarized) and inversely proportional to the pump wavelength [22]. The silica fibers has a very wide Raman gain spectrum up to 40THz due to its amorphous nature. As it is seen in co-polarized case of Fig. 2.8b, the first peak is nearly at 13.2THz and the second peak is at 14.7THz due to non-crystalline nature of silica glass [11]. The multiple peaks exist, since several vibrational modes contribute to the gain spectra. However, the spectra can be modeled by a single peaked function like polynomial, Gaussian or Lorentzian with the loss of some fine structures [23].

As it is mentioned earlier, the stimulated Raman scattering occurs when both pump and probe beams propagate at the same time. The amplification lasts until the frequency shift lies inside the bandwidth of gain spectra. On the other hand, new frequency components can

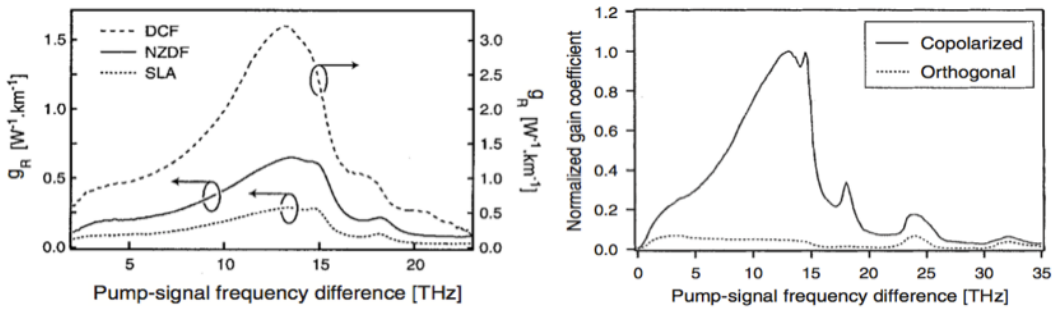

Figure 2.8: Raman gain spectrum of silica fiber and the effect of intensity (a), which depends on the type of fibers and the polarization states (b) on Raman gain coefficient [23].

be generated and amplified by spontaneous Raman scattering, even the initial probe beam does not exist. Although photons within the 40THz bandwidth are generated and amplified, the frequency component which experiences the maximum Raman gain dominates the system due to higher amplification. As a result, in silica fibers, nearly 13.2 THz downshifted Stokes wave is generated. The technique enables to generate 26.4-29.4THz ($\sim$1000cm^{-1}) frequency separated second order Stokes pulses with $\sim$3THz ($\sim$40nm) tunability. This property leads to the design of multi wavelength stable soliton Raman lasers.

For the simplest case, the signal is pumped by single continuous wave (CW) laser, the evolution of pump and the probe beams is governed by the following equations including both the fiber losses and the interaction between them through SRS process [11].

$$\frac{\partial I_S}{\partial z} = g_R I_P I_S - \alpha_S I_S \tag{2.40a}$$

$$\frac{\partial I_P}{\partial z} = -\frac{\omega_P}{\omega_S} g_R I_P I_S - \alpha_P I_P \tag{2.40b}$$

where α_P and α_S are the fiber loss coefficients for pump and Stokes frequencies (ω_P and ω_S), respectively. Additionally, the coefficient $\frac{\omega_P}{\omega_S} > 1$ indicates that the energy supplied by the pump beam is more than the energy gained by the Stokes. Rest of the energy is lost in the system as heat via collisions.

The above differential equations do not have any analytical solution. However, for the small signal case ($I_S \ll I_P$), the pump depletion due to the amplification process can be neglected (first term in Eq. (2.40b)) and hence the solution becomes:

$$I_P(z = L) = I_0 \exp(-\alpha_P L) \tag{2.41a}$$

$$I_S(z = L) = I_S(0) \exp(g_R I_0 L_{eff} - \alpha_S L) \tag{2.41b}$$

where I_0 is the incident pump intensity, L is the propagation length and $L_{eff} = \frac{1-\exp(-\alpha L)}{\alpha}$ is the effective length. The gain term should be greater than the loss term in order to build up Stokes wave inside the fiber. This solution can only be applied for the initial stages of Raman amplification, because the small signal approximation will not be valid for so long due to pump depletion while amplifying Stokes.

2.2.3 Distributed Amplification

A flat gain Raman amplifier, based on stimulated Raman scattering, needs to be designed to provide a uniform amplification for the broadband signal. As mentioned earlier, the fiber becomes the gain medium for the Raman amplification when properly pumped that causes pump depletion due to long fiber lengths [13]. In order to have more uniform amplification along the fiber, bidirectional (hybrid) pumping schemes consist of co-pumping (signal direction) and counter-pumping (opposite direction) may be facilitated, as shown in Fig. 2.9.

The distributed Raman amplification becomes a great alternative to discrete amplification in terms of feasibility, achievable gain bandwidth, uniformity and the signal-to-noise ratio (SNR). The main advantages are as follow:

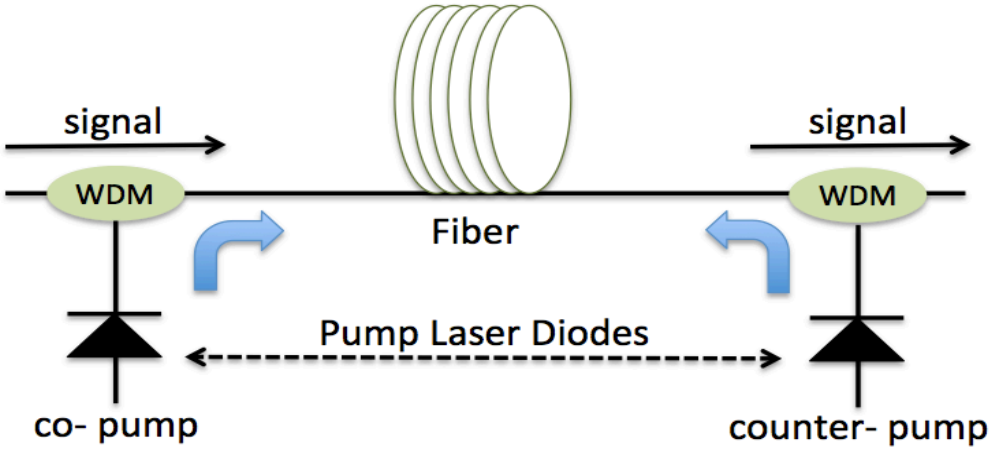

Figure 2.9: The schematics of the Raman amplifier including co/counter pump laser diodes [16].

1. Raman amplification enables fast gain mechanism, since it employs a simultaneous process, SRS [13].

2. Raman amplification keeps the signal level inside the safe region through gain distribution over a long distance. In other words, it prevents the signals to reach high power levels where nonlinear effects are powerful and to drop below the noise floor where noise interference is drastic [24]. Kalyoncu et al. states that distributed amplification provides up to 16dB higher SNR corresponding to 2.5 bit higher resolution in TS-ADC setup [25].

3. Broadband and uniform spectral gain profile can be acquired with using multi pumping schemes and selecting appropriate pump wavelengths and the powers.

The multi-pumped Raman amplifier is modeled by including all signal-to-signal (pump-pump, pump-signal and signal-signal) interactions and the wavelength dependent attenuation (α_k). The following set of equations determines the evolution of all signal and pump powers along the Raman amplified system [16].

$$\pm\frac{dP_k}{dz} = -\alpha_k P_k + \sum_{j=1}^{k-1} g_{\lambda_j}(\lambda_k - \lambda_j)P_j P_k - \sum_{j=k+1}^{N} \frac{\lambda_j}{\lambda_k} g_{\lambda_k}(\lambda_j - \lambda_k)P_j P_k \tag{2.42}$$

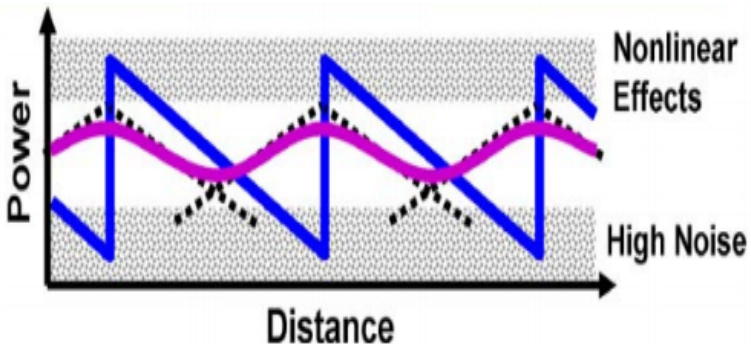

Figure 2.10: The signal level dynamics inside the fiber with discrete (blue) and distributed amplification (red) [24].

where $k = 1, 2, \ldots, N$, +/- corresponds to co/counter propagating signals, P_k is the pump/signal power, α_k is the wavelength dependent attenuation coefficient and g_{λ_j} is the Raman gain coefficient for the signal at wavelength λ_j which is proportional to reference gain coefficient at λ_0 as $g_{\lambda_j}(\Delta\lambda) = \frac{\lambda_j}{\lambda_0} g_{\lambda_0}(\Delta\lambda)$. The first term on the right side of the equation represents the wavelength dependent fiber attenuation. The second term is the gain introduced on the signal at wavelength λ_k by the other signals with higher frequencies, $\lambda_j, j = 1, \ldots, k-1$. The last term, on the other hand, represents the pump depletion on the signal at wavelength λ_k due to power transfer to the other signals with lower frequencies, $\lambda_j, j = k+1, \ldots, N$ [16].

The set of equations above cannot be solved analytically, therefore numerical approaches such as generic and shooting algorithms, are generally used to calculate the proper pump wavelengths and powers to obtain desired uniform wideband gain profile. The Raman Amplifier used in our lab was designed by a senior student [16] using four pumps at 1450nm, 1470nm (forward), 1490nm and 1505nm (backward) in a hybrid pumping setup. Fig. 2.11 shows the gain profile of the designed Raman Amplifier.

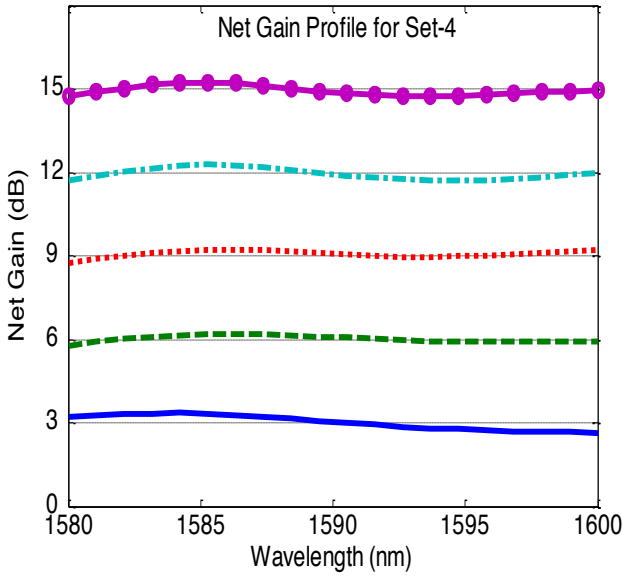

Figure 2.11: The optimized net gain profile of Raman amplifier over 1580nm to 1600nm [16].

Chapter 3

Real-Time Dispersive Laser Scanner

In this chapter, a novel real-time imaging system designed for surface metrology in micro manufacturing is presented. The system employs time-stretching, DMDs and diffraction grating to achieve time, wavelength and space mapping to image the 2D target.

3.1 Introduction

With the advent of micro manufacturing technology, extremely fine surface engineered solids are now reality for higher performance or for new functionalities. For instance, hydrogen fuel cells utilize bi-polar plates with microfluidic channels of dimensions as small as 5μm at the surface to convert fuel into power via electrochemical conversion [26]. In the near future, hydrogen fuel cells are expected to become one of the main alternative energy sources and hence there will be demand for mass production of plates with micro fluidic channels, especially for automotive industry [27]. However, as the mass manufacturing of these micro textured solids becomes reality, the rapid quality control becomes a fundamental bottleneck for high yield.

Characterization of surface texture is an interest of surface metrology and it has been investigated extensively. Up to date several techniques have been developed, mostly specialized on one aspect of the measurement at a time such as measurement of the overall shape, the small-scale features, waviness and the roughness of the surfaces [28]. In general these various surface metrology methods are classified under three categories such as the stylus instruments, scanning probe microscopy, and optical scanning techniques. The first technique, which is based on drawing stylus tip over the surface at constant speed, can enable up to several millimeters wide area with the detection of fine details down to $\sim 1\mu$m [29]. The second technique, which relies on very low contact forces between tip and surface, provides relatively highest lateral resolution ($\sim$1nm) and vertical resolution down to sub nanometers, but lacks of scanning speed and limited to small scanning areas [30]. Optical scanning techniques, on the other hand, measure the surface topography by illuminating the surface through optical system and processing the reflected or transmitted light without destructive physical contact. Among these, interferometric microscopes [31] based on phase shifted interference enable monitoring of wide area with high vertical resolution (<0.1nm) and lateral resolution close to $\sim 0.1\mu$m. Alternatively, confocal microscopy [32], namely a focused beam version of stylus, achieves higher lateral resolution by use of a pinhole, and it is very widely used technique. Higher resolution is achievable by any of these techniques at the expense of scanning area and speed.

Fast laser scanning technology is highly desired in many applications ranging from defense to sensing and micro-manufacturing to increase the imaging speeds [33, 34, 35]. Especially, high speed (>1kHz) scanning is essential for multi-dimensional monitoring of moving objects and to capture fast transient information of a dynamic process pertinent to light detection and ranging (LIDAR) [36, 37], structural dynamics [38, 39], surface vibrometry [40], observation of biomechanical motility [41], cellular network dynamics [42], confocal and multi-photon microscopy [43, 44] applications. In addition, scanning of wide area or many objects in a short period of time is also important for such high-throughput applications as atmospheric

science [36], endoscopy and cytometry for medical diagnosis [45, 46], geographical survey and surface profilometry in the semiconductor industry, and surface characterization and quality control in micro-manufacturing [33, 34, 35]. Various types of laser scanning techniques enabling higher scan rates have been recently proposed. Galvanometric mirrors known as the mechanically scanning mirrors are widely used for beam steering. The scanning speed of such high inertia mirrors is limited to ∼10kHz in 1D and ∼100Hz in 2D [47]. Alternatively, frequency-tunable laser in a diffractive optic bench has recently been demonstrated to achieve more than 10 times higher scanning rates [48]. In addition to the methods mentioned above, new all-optical techniques using acousto-optic deflectors (AOD) are used as a tunable diffraction grating to deflect the beam via electronically changing the angle of 1^{st} diffraction order. Millimeter scale area imaging with $<10\mu$s scanning speed and few micrometer scanning resolution has been achieved [49]. Well known real time dispersive imaging system providing ultra fast frame rates up to tens of MHz combined with a beam deflector to enable 2D wide area scanning has been recently demonstrated [4]. However, AOD is deficient in terms of power transfer efficiency and limited deflection angles, and hence scanning area.

The goal of this project is to demonstrate fast dispersive laser scanning system. Here we achieve ∼20mm^2 wide area scanning with ∼150μm lateral and ∼160μm vertical resolution at 5kHz scanning rate by using DMD technology. DMDs provide alternative fast area scanning technology that can achieve dynamic sectioning of modulated patterns via pixelated MEMS mirrors. Our proposed method using DMD technology can provide fast scanning rates up to 32.5kHz (∼1000 times faster than conventional scanners) and resolution down to single mirror pitch size of 10.8μm with the state of art MEMS technology.

The DMD technology is preferred for real time imaging, because it provides high resolution, high reflection, exceptional stability and excellent controllability over thousands of individual micro mirrors. Also, it has already been commercialized for many applications ranging from confocal microscopy, optical networking, 3D metrology, spectroscopy to medical appli-

cations [50, 51, 52]. By spatially switching the light through micro-mirror arrays, DMD can be utilized as a digital reflective spatial light modulator (SLM). In comparison to most commonly used liquid crystal display (LCD) technology, such devices provide extremely high 2D scanning speeds up to 32.5kHz (<30μs fast switching speed), higher fill factor of 90% than the liquid crystal with 70%, ∼6.6 times higher power transfer efficiency, ∼11 times higher contrast ratio, as twice as higher diffraction efficiency of 88% and feasibility for wide range of wavelengths (UV to NIR) [53, 54].

3.2 Digital Micro-mirror Device

DMD is a pixelated MEMS device created by Texas Instruments with using its extremely powerful and flexible DLP^{TM} technology. It has an array of individually addressable opto-electromechanical pixel units. Each pixel unit consists of aluminum micro-mirror, mechanical assembly and the control electronics, as illustrated in Fig. 3.1. The mechanical assembly includes metal-3 layer, torsion hinge and the yoke. A mirror post connects the micro-mirror to yoke, which is the base for the mirror. The yoke is rotatable over diagonally placed two torsion hinges due to the electrostatic attraction between mirror address electrode on the yoke and yoke address electrode on metal-3 layer. The metal-3 layer lands on the memory cell that consists of metal pads and mechanical stops to determine the maximum rotation angle. Control electronics include CMOS SRAM (complementary metal oxide semiconductor based static random-access memory) cell that keeps the state of the mirror set through a computer software as a binary data (1 or 0). After the CMOS SRAM is loaded with the binary data, the electrodes on the metal-3 layer are charged accordingly to produce electrostatic attraction of yoke and as well the mirror elements to rotate in the specific direction [55].

The maximum achievable frame rate is the fundamental performance parameter of the DMD

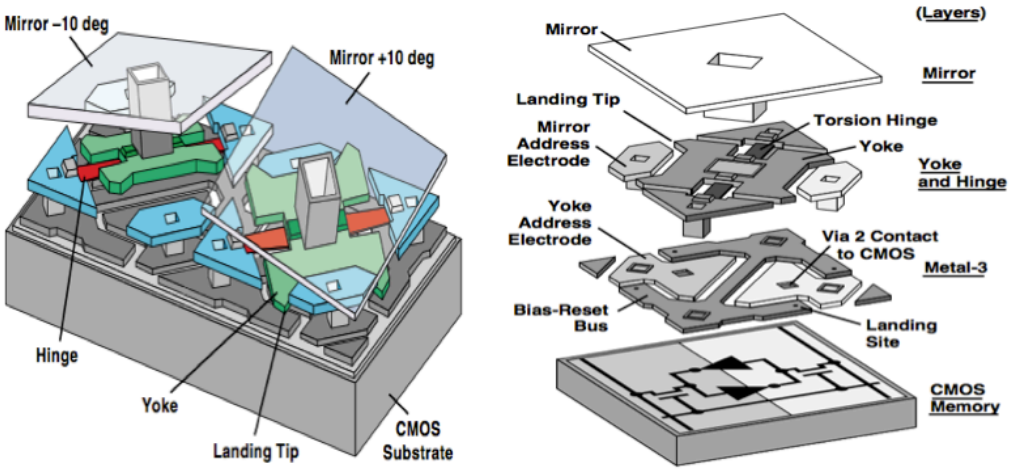

Figure 3.1: The mechanical and electrical control assemblies of the digital micro-mirror memory cell [55].

controller board. The state of the art DMDs can achieve up to 32.5kHz frame rate. Other physical properties such as the array size, maximum tilt angle and the mirror pitch size are tabulated in Table 3.1 for the commercialized current DMD chipsets [56]. As it is shown, while pitch size can go down to 7.56μm, the array size can reach to 1920x1080. In our experimental setup, we have used 0.55XGA chipset with 10.8μm pitch size, 12^o tilt angle, and 1024x768 array size.

Table 3.1: The currently available DMD chipsets from Texas Instruments.

Chipset	Mirror Pitch size	Mirror Tilt angle	DMD Array size
0.17 HVGA	7.56μm	12^o	480x320
0.55 XGA	10.8μm	12^o	1024x768
0.3 WVGA	7.6μm	12^o	608x684
0.7 XGA	13.6μm	12^o	1024x768
0.95 1080p	10.8μm	12^o	1920x1080

3.2.1 DMD Operation

The incident light is reflected through specific directions via tilting the micro-mirrors by controlling the DMD. Each micro-mirror has three different states defined as the flat, ON and OFF. Flat is the default state (neutral position with 0^o tilt angle), when the DMD is switched off, otherwise it cannot be achieved. The other states (ON/OFF) can be achieved according to the loaded binary data into the CMOS SRAM cell. Also, DMD can switch the micro-mirrors between the ON-OFF (+/- $\theta_T = 12^o$) states according to the bit stream [57, 58]. As it is seen in Fig. 3.2, in ON/OFF states, the reflected light deviates +/- $2\theta_T$ degrees from the specular reflection due to the fundamental rule of reflection ($\theta_{inc} = \theta_{ref}$).

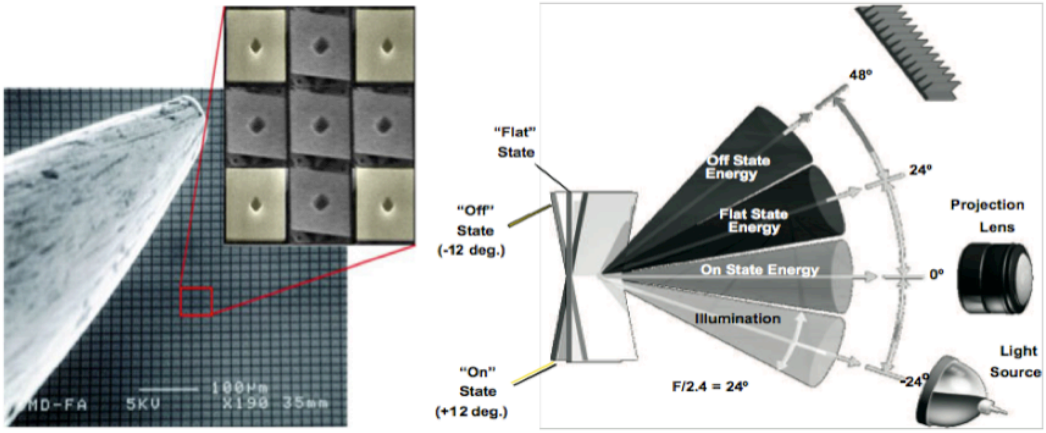

Figure 3.2: The microscopic view (a) of DMD and the micro-mirrors in two different states. The optical function (b) of 12^o micro-mirror tilt device [58].

DMD can be loaded with binary image patterns to create any desired illumination. The binary image patterns can easily be formed in MATLAB via creating 1024x768 matrices with ones and zeros. Gray scale intensities can also be achieved by dynamically switching mirrors with using pulse-width modulation (PWM), besides the black and white projection when the mirrors are statically assigned to a state. In PWM, the pattern is dynamically switched according to the binary code representation to increase or decrease the duty cycle, which will determine the gray scale intensities quantized between 0 and 1, as illustrated in the Fig 3.3. The N bit binary PWM system can be designed to obtain 2^N gray scale

intensities where each ith significant bit covers $\frac{2^{i-1}}{2^N-1}$ percentage of time [55, 59]. However, the DMD is used as a beam steering device in order to scan a wide area as line-by-line.

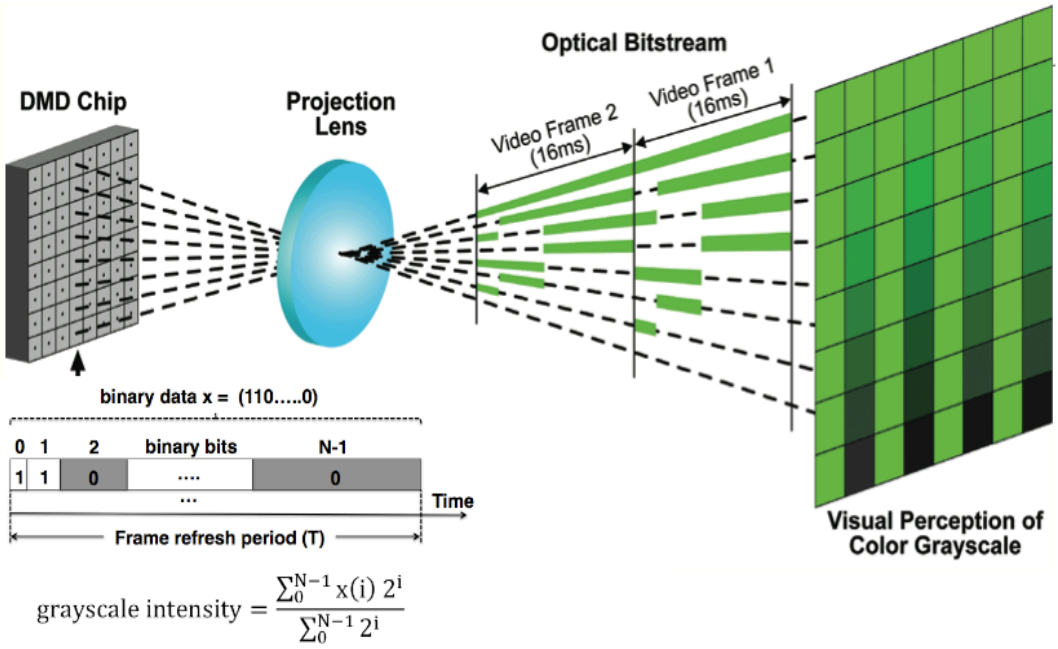

Figure 3.3: The binary N bit PWM system designed to obtain grayscale intensity levels [59].

3.2.2 DMD Properties: Advantages and Disadvantages

DMD is a micro-optical device designed to be used as a digital spatial light modulator by providing much better optical performance in terms of speed, feasibility for broadband illumination, active area, contrast ratio and the diffraction efficiency than the other types of SLMs [54]. The main advantages and the disadvantages of the DMD in comparison to most commonly used liquid crystal display (LCD) technology are listed below:

Advantages :

1. With the state-of-the-art MEMS micro-mirror technologies, up to 32.5 kHz pattern rate with a fast switching speed of less than 30μs between the states, allows fast display of illumination patterns. On the other hand, LC based SLMs can achieve at most the time scale of milliseconds.

2. The LC-SLM is a transmissive device, however the DMD is reflective. While the light is transmitting through the cascaded glass layers, it experiences more attenuation due to back reflection and absorbtion. On the other hand, reflective DMD surface consists of tightly builted micro-mirrors with $\sim$1μm gap that provides higher fill factor (ratio to pixel size of 10.8μm) of 90% than the LC-SLM with 70%.

3. The DMD can provide 6.6 times higher power transfer efficiency, that is the ratio of reflected irradiance to incident irradiance, than the LC-SLMs. As a result, DMD becomes more suitable for high power applications and same irradiance can be achieved with less exposure time.

4. The DMD performs $\sim$11 times and $\sim$3.3 times higher contrast ratio between maximum and minimum fluxes at the diffuser, for projected and holographic images, respectively.

5. The DMD generated images show slight artifacts mainly at the edges of micro-mirrors, however the LC-SLM generated images show much noticeable artifacts due to interference of multiple reflections from cascaded glass layers of the LCD.

6. The pixelated structure of both DMD and LC based spatial light modulators functions as a diffraction grating. The tilted surface due to states of micro-mirrors turns the DMD into a blazed diffraction grating with a blaze angle of θ_T (tilt angle). Thus, when illuminated at blaze angle (blaze condition $\alpha = \beta$) as twice as higher diffraction efficiency of 88% can be obtained than the LCD device.

7. DMD's mirrored surface can enable modulation of broadband light ranging from ultra-violent (UV) to near infra red (NIR). The DMD mirrors are also protected by a cover glass, which is coated to operate for desired spectral window [16].

Disadvantages :

1. The DMD can enable only amplitude modulation, since it only has a reflective mode. However, the LC-SLMs can be used both in reflective and transmissive modes that facilitate both amplitude and phase modulation.

2. The DMD mirror array as a 2D blazed diffraction grating with period of mirror pitch size (typically 10.8μm) distributes the incident beam into diffraction orders. The state of the micro-mirrors has no effect on the diffraction grating, only changes the corresponding power distribution over the diffraction orders. The diffractive nature of DMD causes degradation in the coupling efficiency and the higher diffraction orders create interference patterns, which appear as background noise, for especially broadband applications [16, 54].

3. The 2D diffraction grating nature of the DMD arrays also cause wavelength separation in vertical axis when more than single line is used to steer the beam due to power limitations. Since we are employing cylindrical lens to stop the spatial separation of wavelengths, unwanted vertical separation is not corrected. It causes tilted lateral scan on the target that is clearly seen in Figure 3.9c. This can be easily corrected by rotating the scanner head or the scanned target. However, due to long distances ($\sim$60cm) from the DMD to the target, some wavelengths of the returned signal may be filtered out if they miss the DMD's ON portion.

3.3 Experimental Setup and System Description

Figure 3.4 illustrates the concept of novel 2D imaging system utilizing MEMS DMD technology. Ideally large area scanning is achieved by using N pulsed lasers with the same repetition rates. Each laser will send optical impulses to image different subsection of the imaging plane. Since detection system uses single photodetector, each pulse is generated with a constant delay, $n \times \tau, (n = 1, 2, 3, \ldots, N)$, where $N \times \tau \leq T$ =repetition rate. In the proposed system, N lasers array is replaced by a modelocked fiber laser as a master light source to generate broadband supercontinuum of light through nonlinear process [60]. Specifically, supercontinuum pulses are generated to provide broadband source by propagating the Mode Locked Laser pulses (at 1550nm with <1ps pulse width and 20MHz repetition rate) through a fiber-based system that consists of an EDFA and the cascaded single mode, dispersion shifted and nonlinear fiber patch cords. Band pass filter (CWDM) centered at 1590nm is used to carve out ∼20nm nearly flat portion of the spectrum for scanning. In the first stage, carved SC pulses are wavelength-to-time mapped by using a dispersion compensation module with dispersion (D= -675ps/nm) for real time detection. In this step, group velocity dispersion is being used to create a time delay between different colors of the pulse and hence spread spectral content linearly in time domain. The timing requirement at this stage is imposed by the overlap between lasers after time stretching. The delay between consecutive pulses (τ) should be larger than the chirped pulse width at the input of the circulator [2, 61, 62]. A pulse picking setup using optical switches follows the SC source and time wavelength mapping process to generate N parallel optical paths and to mimic the N independent lasers. After time wavelength mapping, selected pulses are launched into free space by an array of collimators and followed by DMDs to facilitate 1D scanning. The optical pulses, on the other hand, are highly attenuated while passing through the system. The system losses are mainly due to the DCM (∼2.1dB insertion loss) and the DMD which induces single pass attenuation of ∼45% by considering the beam wavelength (1590nm),

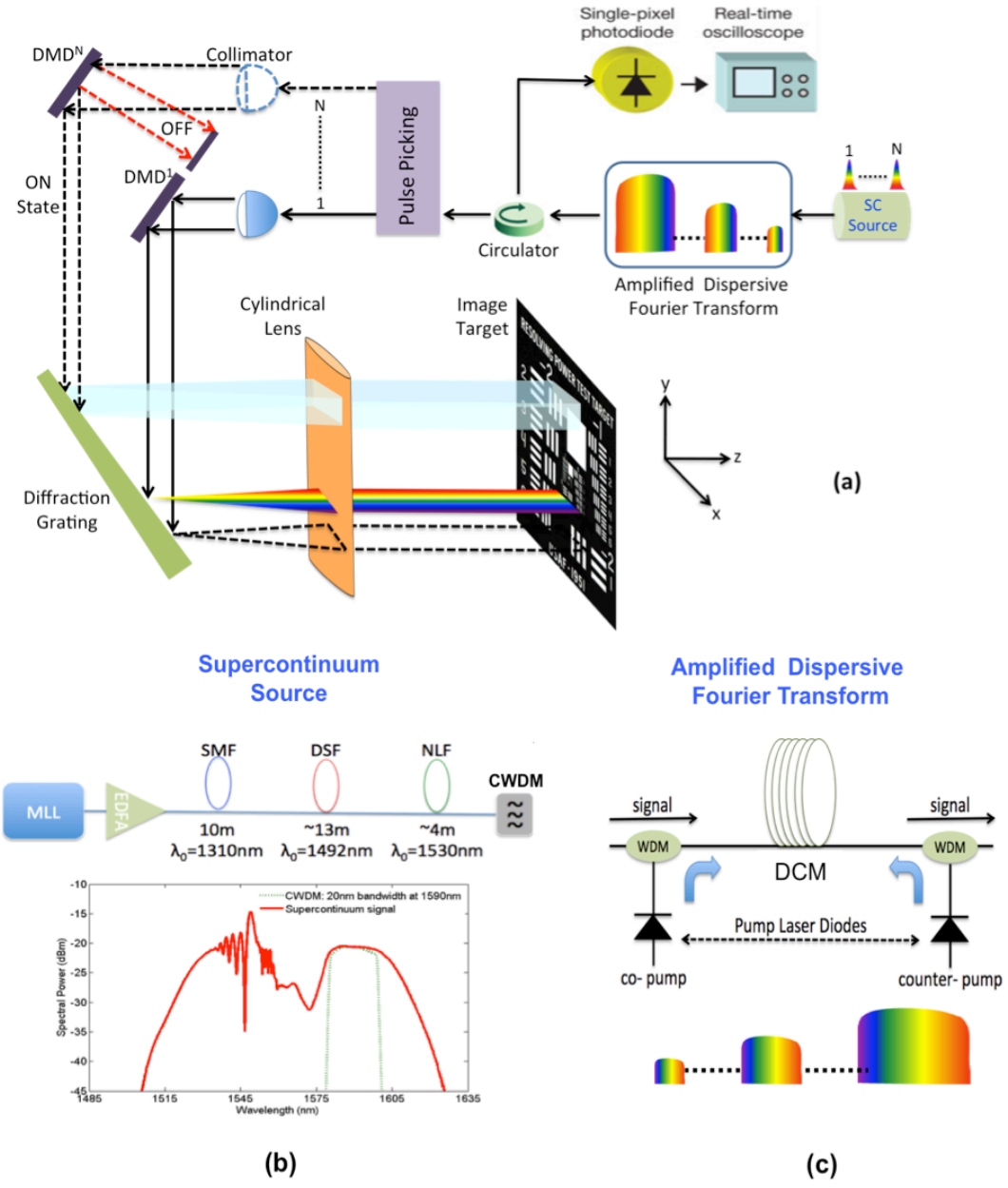

Figure 3.4: The experimental setup for all optical reflective parallelized N-channel dispersive laser scanner (a). The single channel setup is used for the proof-of-concept demonstration. The supercontinuum pulse generation (b) and the amplified dispersive Fourier transform (c) modules.

micro-mirror reflectivity (∼90%), active area (∼90%), diffraction efficiency (88%) and the protective cover glass on the micro mirrors (single pass transmission coefficient of ∼90% if coated for NIR and ∼75% if coated for visible) [39]. In the experimental setup, since power budget was not sufficient for simultaneous multichannel measurement, only one channel at a time has been used for scanning. Also, in order to compensate the system losses and to obtain a better signal to noise ratio, a flat gain Raman amplifier is designed to provide a uniform amplification through the DCM. The Raman amplification with ∼10dB net gain and <0.5dB gain ripple is introduced by using four pump diode lasers at wavelengths of 1450nm, 1470nm, 1490nm, and 1505nm in a hybrid pumping configuration.

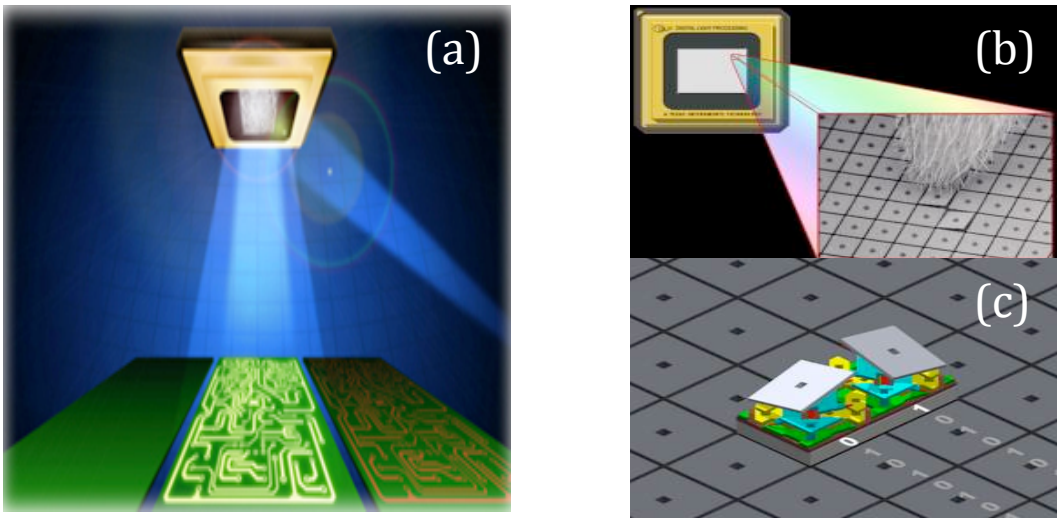

Figure 3.5: DMD as a programmable beam steering technology (a) [63]. A single DMD consisting 768x1024 micro mirrors and inset shows the SEM image of micro mirrors (b). Schematics of individual micro mirrors (c) [8].

In the second stage, the optical beam is expanded to illuminate the active area of the DMD, which consists of individually controllable micro mirror arrays. Here, we use DMD mirrors fabricated by Texas Instruments. By switching the state of individual micro mirrors from ON state to OFF state, the large optical beam is digitally divided into segments and mapped to different locations at the image plane and hence beam steering is achieved as shown in Fig. 3.5. The spectral content of the time stretched SC pulses is dispersed by the diffractive optics which is composed of a blazed diffraction grating and a Fourier lens to illuminate

each location in space by different colors of light that arrive at different times. After being mapped over the focal plane, the spectrum of the pulses is modified by the reflection and transmission property of the target image. Through the time wavelength mapping process that was achieved in fibers, the spectral modulations are mapped to the time domain at the image plane. The spectrally and temporally modulated pulses via DMD are then captured by a photo detector (>1.2GHz bandwidth), which is placed at the optical path that corresponds mirrors' ON state direction, while at the OFF state, beams are blocked by the setup. A real time storage oscilloscope with 8GHz RF bandwidth captures the electrical signals from the photodetector for post processing.

3.3.1 Lateral Scanning

The broadband optical pulses are spatially dispersed and focused over the space by using diffractive optics including diffraction gratings and Fourier lenses. Due to the pulse nature of the illumination, image modulation is captured by a single pulse and thus the lateral scanning rate is in megahertz, which is determined by laser repetition rate. The normalized intensity distribution $\bar{I}(x,\lambda)$, field of view (FOV) and the spatial (Δx) resolution of the pulse shaping system for both plane waves $E_p(x,d) \propto rect(x/d)$ and Gaussian waves $E_g(x,w) \propto exp(-0.5x^2/w^2)$ where $w = d/(2\sqrt{\ln 2})$ are calculated as [8]:

$$Gaussian : \bar{I}(x,\lambda) = \exp^2\left[-\frac{\pi^2(x-x_0)^2}{2\ln 2\lambda^2}\left(\frac{d}{f}\right)^2\right] \tag{3.1a}$$

$$Plane : \bar{I}(x,\lambda) = sinc^2\left[\frac{x-x_0}{\lambda}\left(\frac{d}{f}\right)\right] \tag{3.1b}$$

$$Gaussian : \Delta x \approx \frac{2\lambda f}{d\pi}\ln 2 \tag{3.1c}$$

$$Plane : \Delta x \approx \frac{2\times 1.39156\lambda f}{d\pi} \tag{3.1d}$$

$$FOV \approx G_\beta f \Delta\lambda \tag{3.1e}$$

Here f is the lens focal length, d is the beam size, $x_0 \simeq G_\beta f(\lambda - \lambda_0)$ is the relative position of 1^{st} order diffraction peak with respect to central wavelength (λ_0) and G_β is the effective groove density, which is defined as a function of 1^{st} order diffraction angle, $G/\cos(\beta)$ [8]. The beam size is defined as the aperture size for plane waves, and full width at half maximum for Gaussian beams. The 1^{st} order diffraction angle (β) for the incident beam at wavelength (λ) and the incident angle (α) is calculated by using the grating equation as $\sin(\alpha) + \sin(\beta) = \lambda G$ which reduces to $2\sin(\beta) = \lambda G$ in a Littrow configuration ($\alpha = \beta$).

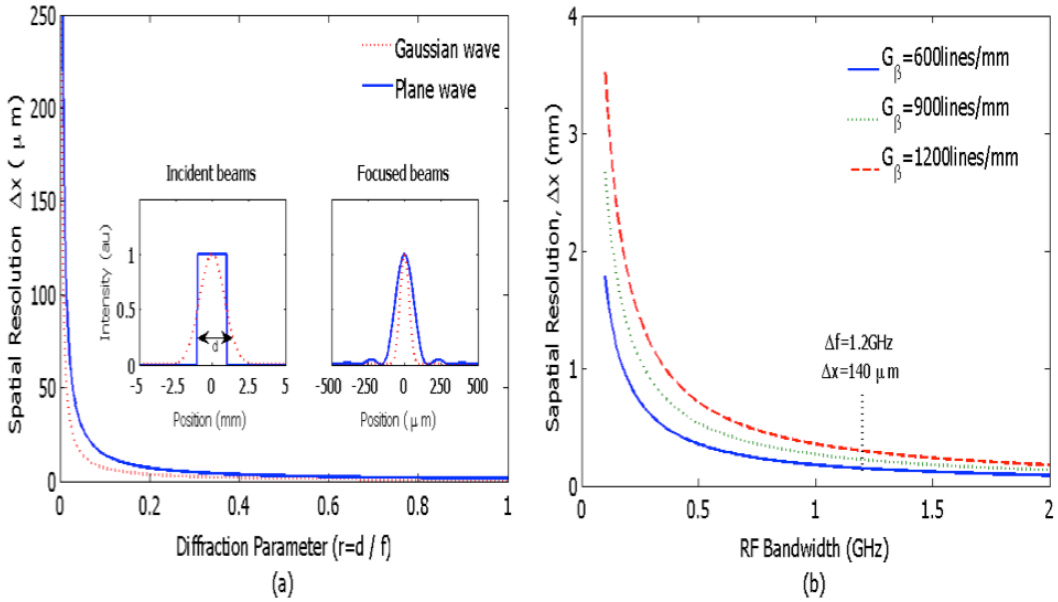

Figure 3.6: The spatial resolution of the focusing system depends on the diffraction limit and is impoved by increasing diffraction parameter, r=d/f (a). The temporal resolution (calculated for D= -675ps/nm) due to the RF bandwidth limits the spatial resolution via time-to-space mapping (b) [8].

Final resolution of the imaging system is defined not only by the diffraction limit but also by the temporal resolution (bandwidth) of the detection system. Figure 3.6 illustrates the achievable resolution with respect to key parameters of optical components and the RF detection system. According to Eq. (3.1d), the system resolution is optically limited by the diffraction limit ($r = d/f$) due to Fourier optics. By increasing the diffraction parameter ($r > 0.1$), the spatial resolution $< 10\mu m$ is achievable, as illustrated in Fig. 3.6a. In this proposed system, by changing the number of horizontal mirrors, DMD can enable tunability of the

beam size and hence the diffraction limit. The lateral resolution of the system is mainly limited by the detection system. A photodetector with a given RF bandwidth (1.2GHz used in our experiments) limits the achievable temporal resolution ($\Delta t_{det} \approx 1/\Delta f$) to ~800ps which corresponds to spectral resolution ($\Delta\lambda_{det} \approx \frac{1}{\Delta f \cdot D}$) of ~1.2nm (due to uniform $-675 ps/nm$ dispersion) which translates into a spatial resolution of, $\Delta x_{det} \approx \frac{G_\beta f}{\Delta f \cdot D}) \approx 145\mu m$, via time-to-space mapping, as illustrated in Fig. 3.6b.

3.3.2 Vertical Scanning

In our proposed 2D imaging system, the vertical scanning is achieved by a DMD that is used as a beam steering device. At each vertical position, SC pulses directly capture the entire lateral image by using spatio-temporal dispersive imaging technique without scanning. The lateral resolution (Δx) is determined by 4-f imaging system, which consists of diffraction grating and a Fourier lens in a double pass system, and the resolution estimated by the width of the focused beam through Eq. (3.1d). Spatially and spectrally shaped pulses are then stretched over time by passing through the highly dispersive DCM for real time detection.

Figure 3.7 illustrates the sample binary patterns created on DMD for beam steering. In these horizontal strip-type patterns, the white parts correspond to NxM arrays of ON state mirrors and the black parts correspond to OFF state mirrors. In the imaging experiment, first such horizontal strip patterns on DMD, namely narrow spatial masks, are created and then the light reflected by the mirror array is sent onto the object through a cylindrical lens. The vertical scanning is achieved by dynamically shifting this mask at the DMD, which, as a result, shifts the reflected light onto the object. Consequently, the vertical (Δy) resolution is expected to be different from what is estimated by the Eq. (3.1c). Indeed, it is determined by the number of rows of mirror arrays that switch to the same state simultaneously or the size of masks on DMD surface. Hence, a use of N rows will create an optical beam where

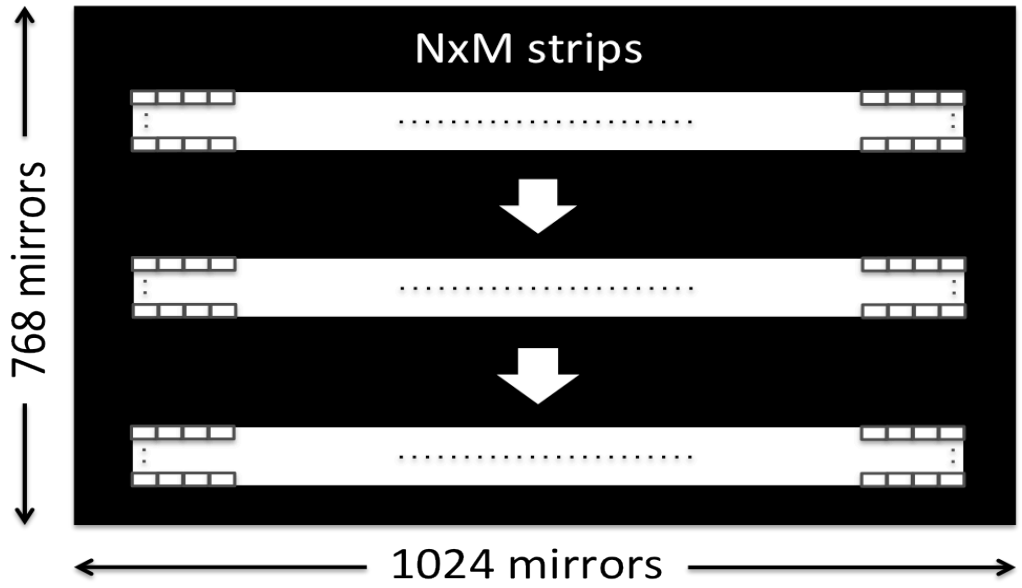

Figure 3.7: The horizontal strip-type binary patterns created on DMD for laser scanning. The position of the NXM spatial mask is vertically scanned over the object by loading DMD with these dynamic patterns.

the vertical beam waist will be $N \times 10.8\mu m$, where 10.8μm is the mirror pixel size at the DMD chip. Increasing the number of rows in DMD array increases the SNR, since more optical power is reflected on to the object. However, it will decrease the vertical resolution, since the width of the reflected light on image increased. The vertical scanning speed is the second crucial parameter in the proposed experimental system and it is determined by the frame rate of DMD. Experimentally, DMDs with 32.5kHz scanning speed ($\sim 30\mu$s switching time) can achieve $\sim$600 laser pulses to illuminate the same subsection or 600 subsections for pulse picking at the same laser pulse rate (20MHz / 32.5kHz).

3.4 Experimental Results

Real time imaging can work in reflection or transmission mode. To demonstrate 2D fast scanning capability, we used the time-space-wavelength mapping technique working in the reflection mode. The target image scanned by the DMD is recorded by the series of SC

pulses. This 1D pulse stream (stream of horizontal line scans) with 50ns time aperture is then segmented for different vertical coordinates, vertically aligned and digitally processed to extract the spatial features and reconstruct the original 2D image.

In this experimental study, we have used optical beam with ∼5mm beam size, diffraction grating with 600lines/mm, lens with 200mm focal length, DMD (0.55-inch diagonal mirror arrays, 1024x768 individually addressable aluminum micro mirrors, 10.8μm pitch size, discrete states of ON (+12^o rotation) or OFF (-12^o rotation), and frame rate of 5kHz) and 15×600 horizontal excitation strips to vertically scan the target image (USAF test chart) which consists of vertical black and white strips with different spatial frequencies. The proposed system can scan ∼20mm^2 wide area [∼3mm lateral ($FOV_{lateral} = G_\beta f \Delta\lambda$) and ∼7.6mm vertical ($FOV_{vertical} = 768 \times 10.8\mu m$) with 20MHz (pulse repetition rate) in 1D and 5kHz (DMD frame rate) in 2D.

Figure 3.8 illustrates the lateral resolution performance of the dispersive imaging system. The 2D image of five groups of vertical bars with dimensions varying from ∼150μm to ∼220μm is captured by our dispersive laser scanner. The temporal modulation (due to spatial/spectral pulse shaping) of the SC pulses by the vertical bars with varying spatial frequencies is shown in Fig. 3.8. Due to the diffraction limit of the focusing system, as the spatial frequency of the patterns increases, the modulation depth decreases. Thus, we used vertically wider excitation strips (N=15 mirrors) to increase the signal to noise ratio at the expense of diminishing vertical resolution to ∼160μm compared to 10.8μm vertical resolution that is achievable by using narrow strips of N=1. In addition, vertically wider strips shifted by certain number (n<N) of pixels (overlapping strips) can be used to increase the SNR and to achieve higher vertical resolution (n × 10.8μm).

Figure 3.9 compares the 2D CCD image and the reconstructed images of the test target (Fig. 3.9a: USAF test chart) captured by our MEMS based dispersive laser scanner. The image is reconstructed by mapping the reflection from the target encoded on the pulse train at

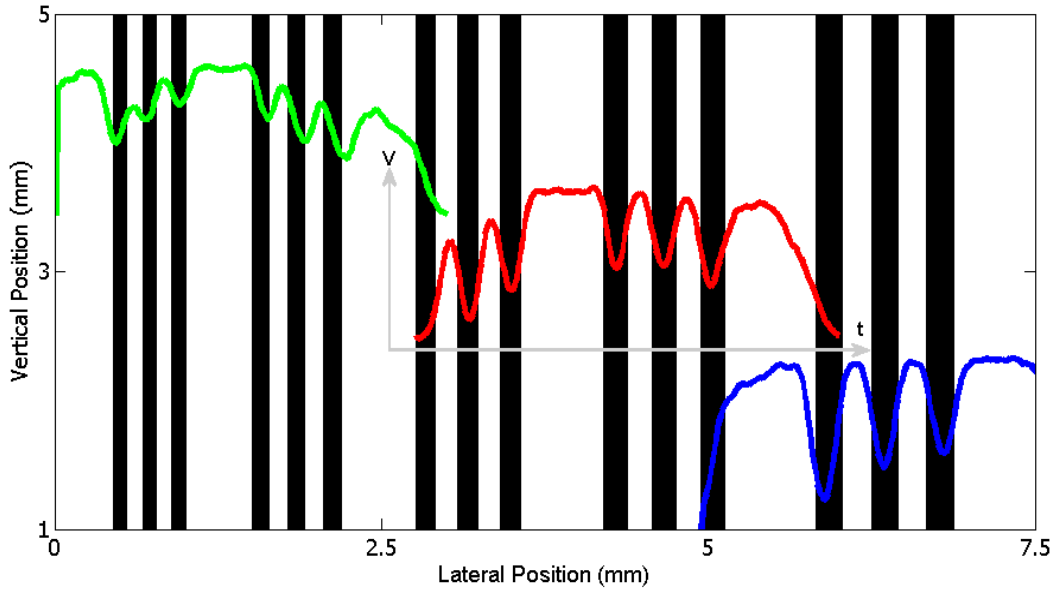

Figure 3.8: The lateral resolution performance of space wavelength mapping. The vertical bars with dimensions of ∼150μm to ∼220μm are captured by the ∼13.5ns SC pulses.

different scanning positions into a 2D matrix. Dynamically shifting the 15×600 excitation strips over the DMD at 5kHz rate, the target is scanned with a resolution of ∼150μm (lateral) and ∼160μm (vertical). The captured image clearly shows the vertical and horizontal bars: Group=1, Element 3-6 (Fig. 3.9b) and Group=0, Element 5-6 (Fig. 3.9c).

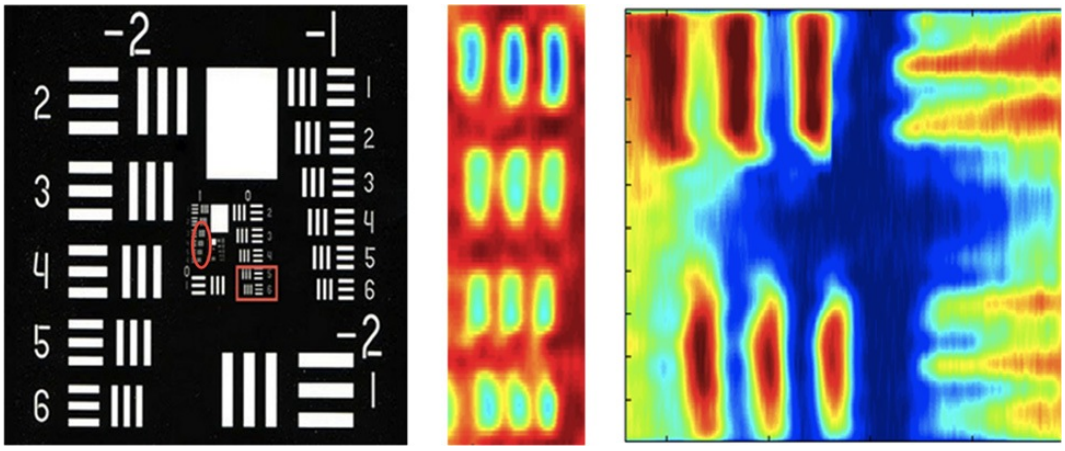

Figure 3.9: Comparison between a CCD image (a) and a digitally reconstructed scan image of the target: USAF test chart Group=1, Element 3-6 [width / line 198μm-140μm] (b) and Group=0, Element 5-6 [width / line 314μm-280μm] (c).

To construct the image the normalized intensity distribution $\bar{I}(x,\lambda)$ calculated in Eq. (3.1a)

is nearly same for all the wavelengths within 20nm spectral window centered at 1590nm (λ_0). Thus, the intensity distribution for each wavelength is approximated as:

$$\bar{I}_0(x) \simeq \bar{I}(x, \lambda_0) \tag{3.2a}$$

$$I(x, \lambda) \simeq F(\lambda) \cdot \bar{I}_0(x - x_0) \tag{3.2b}$$

where $I(x, \lambda)$ is the intensity distribution and $F(\lambda)$ is the spectral power density. The space-to-wavelength mapped optical beam is both spatially and spectrally shaped by the target image m(x), which can be modeled as a convolution at Fourier plane.

$$y(\lambda) \simeq F(\lambda) \cdot \int_{-\infty}^{\infty} \bar{I}_0(x - x_0) \cdot m(x) dx = F(\lambda) \cdot conv[I(x, \lambda), m(x)] \tag{3.3}$$

Spectrally encoded signals are converted into time domain $\left[y(\lambda) \xrightarrow[mapping]{frequency-to-time} y(t) \right]$ via dispersive Fourier transformation through highly dispersive fibers. By neglecting the higher order dispersion terms, namely assuming a uniform dispersion over a wide spectrum, the temporal mapping is modeled linear as $\Delta t = D \cdot \Delta\lambda$ where Δt is the temporal position of the wavelengths relative to the reference wavelength. By using such digital signal processing techniques as digital filtering and deconvolution, the spatial information of the target, m(x), can be extracted.

The system performance of current experimental approach of this real time imaging, however, is limited in terms of the spatial resolution, field of view and the power efficiency due to following reasons. The diffraction prevents the use of bulk Fourier lenses with long focal lengths ($\propto \lambda f/d$) and hence limits the spatial resolution. Also, 1cm^2 active area of the DMD combined with diffraction gratings ($\sim 3.5^o$/100nm spatial dispersion with 600lines/mm groove density) limits the field of view. Finally, high losses due to higher order diffractions limit the power efficiency of the system. In order to achieve resolution close to 20μm and lower, the system should be able to illuminate the whole imaging sample with frequency-time

and space-time mapped light, focus the light everywhere on the sample to <20μm spot size and should be low loss for high contrast imaging. Furthermore, in order to make the system compatible with manufacturing technology the working distance should be long, >0.5mm to avoid contact and contamination. Planar optical devices such as lenses or diffraction optics combined with real time imaging can facilitate high resolution imaging in real time.

3.5 Conclusion

We have proposed a fast dispersive laser scanning system by using MEMS micro mirror technology. Two-dimensional beam steering is employed by combining the space wavelength mapping for the lateral scanning and digital micro mirror arrays for vertical scanning. By dynamically switching the states of the micro mirrors, the position of the spatially dispersed beam is moved over the target. We have monitored $\sim$20mm^2 wide area with $\sim$150μm lateral and $\sim$160μm vertical resolution for the proof of concept. We estimate that MEMS based amplified time stretched system can achieve fast vertical scanning with frame rates up to 32.5kHz and with resolution down to single mirror pitch size of 10.8μm.

Chapter 4

Scalability Approaches

In this work, by the help of dispersive fourier transform and 1024x768 individually controllable digital micro-mirror arrays, we scanned $\sim$20 mm^2 wide area experimentally at a scan rate of 5 kHz and achieved $\sim$150μm lateral and $\sim$160μm vertical resolution. The laser scanner system can be improved in terms of scan area, speed, power, and resolution. In this chapter, we will provide the trade-offs between these performance parameters and ideas on how we can improve the system to achieve larger area scan with faster scan rates and higher resolution while optimizing power.

4.1 Scanning Area Improvement

In the proposed system, as discussed in Chapter 3, vertical scanning is directly controlled by DMD and lateral scanning is controlled by wavelength to space mapping due to diffraction grating and the focal length of cylindrical lens that stops the wavelength separation in spatial domain. Therefore, in order to increase scanned area, both vertical and lateral distances should be increased. However, there are trade-offs between lateral scan area and

lateral resolution due to time-space-wavelength mapping. Since, our amplified DFT system and detection system is not changed, increasing lateral scan area by using more powerful diffraction grating (e.g. G=1200 lines/mm groove density), will decay the lateral resolution with the same amount. Because while FOV is linearly proportional to the groove density, lateral resolution (Δx) is inversely proportional as shown in Equation 4.1.

$$FOV \approx \frac{G}{cos(\beta)} f \Delta\lambda \tag{4.1a}$$

$$\Delta x \approx \frac{Gf}{cos(\beta)\Delta f D} \tag{4.1b}$$

where G is groove density of the diffraction grating, β is the 1^{st} order diffraction angle, f is the focal length of cylindrical lens, Δf is detector bandwidth and D is the dispersion parameter that facilitates time to wavelength mapping in the system. Due to the trade-off between lateral scan area and resolution, it is not straightforward to improve the width of the scan area. System should be optimized according to the need.

On the other hand, vertical resolution is limited by the individual micro-mirror size of DMD, therefore it is fixed at $10.8\mu m$ when we overcome the power limitations to facilitate single line scan. However, in practice, we employed 15 line scan to have good SNR at the detector. If we can keep the same power level on the DMD, vertical scan area can be improved easily by cascading several DMDs without sacrificing the vertical resolution.

Figure 4.1 is showing the proposed system to increase the height of the scan area. Since the area of diffraction grating and cylindrical lens can easily be increased, when we cascaded the DMDs, we need only extra DMDs and a pulse picker device which is another beam steering equipment that will reroute the incoming beam to different DMDs, hence different scanning regions. Such beam steering device should have large deflection angle, but does not need to be as fast as DMDs. In the ultimate scan with single line resolution of $10.8\mu m$, each DMD will make 768 scans before switching to the other DMD. Therefore, even for the fastest

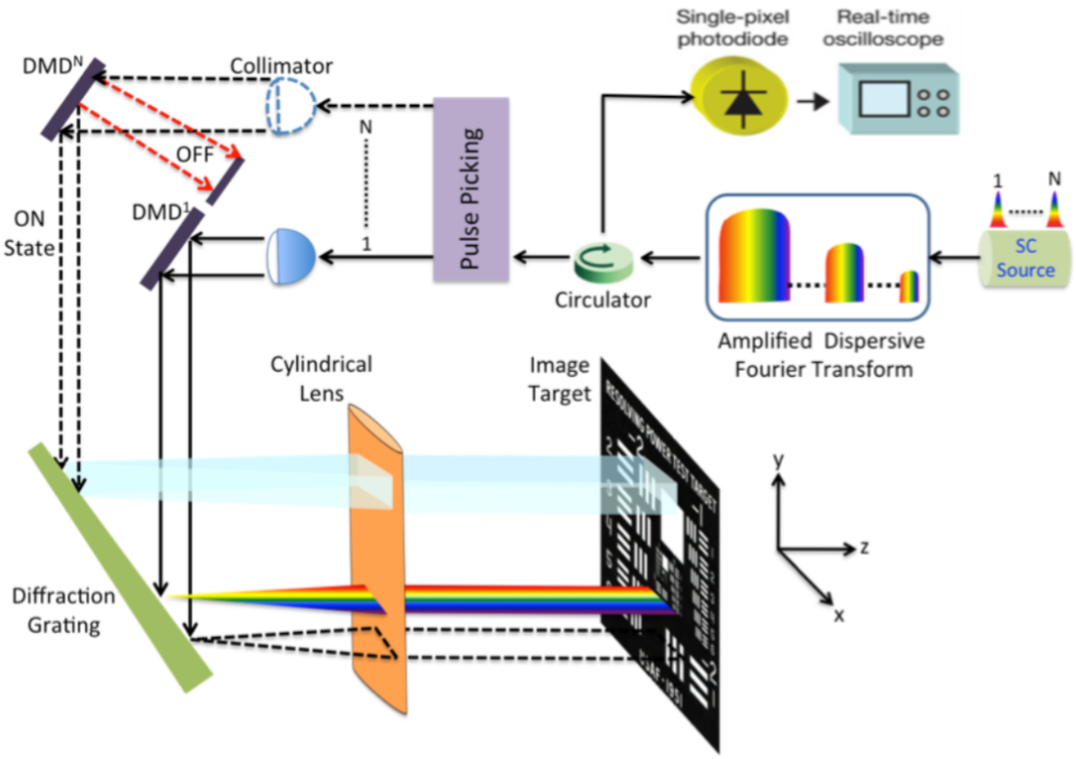

Figure 4.1: The experimental setup for all optical reflective parallelized N-channel dispersive laser scanner

DMDs, the required speed is less than 50Hz which is easily achievable by several devices from liquid crystals to galvonometric mirrors. In this approach, DMDs are cascaded in a sequential scheme, therefore scan area can be improved, but scan speed stays same.

On the other hand, one can facilitate acousto-optic deflectors (AOD) as a pulse picker to achieve parallel scan and speed up the vertical scan. Even though, AODs achieve up to 200MHz scan rates, they have limited deflection angles (<60mrad), therefore the distance between pulse picker and DMDs should be long to achieve enough separation. Therefore, system will not be compact and power transfer efficiency will decrease. Also, since the scan will not be linear, post-processing will be slightly more complex. In this parallel scheme, while DMDs are changing the scan pattern, hence scan region, AOD will reroute the beam to other DMDs and all of them will finish scanning first portion of the area before passing to the next pattern.

4.2 Power Efficiency Improvement

In the current system, the peak power of the signal is decaying either due to loss or redistribution of total power to larger bandwidth, longer time or larger area. First of all, supercontinuum generation is a lossy process, because femtosecond pulses that has 3-4nm bandwidth is expanded through nonlinear processes to achieve broadband spectrum (>200nm). Later, only 20nm flat region of such broad spectrum is carved to be used in the system. Therefore, the power efficiency of supercontinuum generation is below 10%. After MLL, a C-band EDFA is employed to increase pulse intensities that will utilize the nonlinear processes in the fibers which are used to generate supercontinuum source. On the other hand, dispersive fourier transform is facilitating time-wavelength mapping, therefore initially overlapping wavelengths are distributed in time. Even though, insertion loss of such system is <3dB, due to temporal redistribution of energy, peak intensities are decreased drastically. In the system, in order to compensate such losses, we employed Raman amplification on the dispersion compensation module (hence we call it Amplified DFT). The dispersion compensation module is pumped with four diode lasers at wavelengths of 1450nm, 1470nm, 1490nm, and 1505nm in a hybrid pumping configuration and ∼10dB net gain with <0.5dB gain ripple is achieved. Therefore, the losses in the fiber-based system are well compensated by the EDFA and Raman amplifiers.

Additionally, another EDFA with ∼20dB gain is used to partially compensate the losses that will be caused by the upcoming free space components that are i) digital micro-mirror device, and ii) diffraction grating. The loss of each system is coming from the nature of their usage.

First, we are facilitating DMD as a beam steering device that selects only a small stripe of the beam to achieve high vertical resolution. In the case of facilitating ultimate resolution of $10.8\mu m$, we are selecting only one line out of 768 lines. Therefore, when we assume uniform

illumination and consider ∼85% fill factor and ∼90% mirror reflectivity, the power transfer efficiency of the DMD will be as low as 0.1%, hence ∼30dB loss is occurred. Therefore, we are using 15 lines wide strips and improve signal level 11.76dB in order to improve SNR with the same amount, however we sacrifice from the vertical resolution. In this way, we also somewhat equate the vertical and lateral resolutions of the system. As discussed earlier in Chapter 3, the achievable lateral resolution is 140μm, so choosing 15 lines wide strips (∼160μm wide) for vertical scanning somewhat equates the resolutions in both dimensions.

On the other hand, the loss of diffraction grating is caused by the energy distribution on different diffraction orders. The diffraction grating equation is simply,

$$a[sin(\theta_m) + sin(\theta_i)] = m\lambda \tag{4.2}$$

where a is the distance between grooves of the diffraction grating, m is the order of diffraction, θ_i is the incident angle and θ_m is the diffraction angle for the order m and wavelength λ [64]. The angles are measured with respect to the grating normal and θ_i is assumed positive all the time, therefore θ_m is negative if the incident and diffracted beams are on opposite sides of the grating surface normal, as illustrated in Figure 4.2. If the beams are on the same side of the grating normal, then both angles are considered positive [65].

The conventional gratings suffer from the fact that the zeroth order mode, that has the maximum grating efficiency, contains no diffraction pattern and appears as a surface reflection. As it is clearly seen in Eq. (4.2), specular reflection ($\theta_m = -\theta_i$) is only possible at m=0 where the diffraction angle is independent of wavelength or gratings spacing. Therefore, all the power transferred to this zeroth order is considered as loss. This issue can be resolved by creating a repeating surface pattern, which produces a different surface reflection geometry as in blazed gratings shown in Figure 4.2.

The blazed grating is a specific form of diffraction grating that is designed to produce the

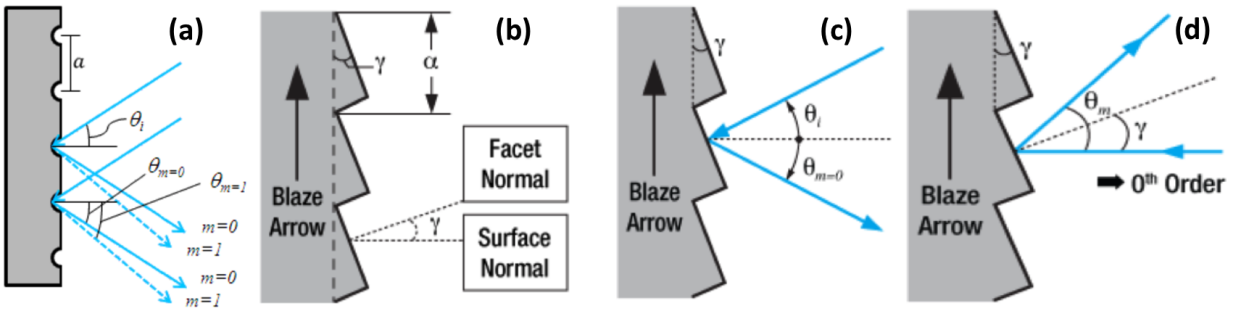

Figure 4.2: (a) Conventional reflective grating (b) Blazed reflective grating with blazed angle γ (c) Reflection of zeroth order (d) Specular reflection is matched to the diffraction order m≠0 ($\theta_m = 2\gamma$) [65]

maximum grating efficiency in a specific diffraction order other than zero. In this way, the majority of the optical power is transferred to the designed diffraction order while minimizing power lost to other orders. However, this design limits the operation of the blazed grating to a specific wavelength, known as the blaze wavelength. Another important characteristic of blazed gratings is the blaze angle γ that is the angle between the surface structure and the surface parallel. Blazed gratings follow the same diffraction grating equation where the angles are defined with respect to the surface normal of the grating. However, the specular reflection is happening according to the facet, hence related to the blaze angle. Therefore, the diffraction efficiency at the specific order can be manipulated by varying the blaze angle. Simply, the grating is engineered to match the specular reflection to a higher diffraction order where wavelength separation is possible. Generally, first diffraction order is facilitated in blazed gratings due to efficiency and free spectral range decrease at higher orders.

In order to improve power efficiency of our imaging system, we employed two different blazed gratings. First one is a commercial grating from Thorlabs designed for 1.6μm with 600 grooves per mm and 28^o 41' blaze angle that can provide 1.46nm/mrad dispersion. Other one is a phase-gradient gap-plasmon metasurface (GPM) based blazed grating operating at 1550nm [66] that is designed, fabricated and and characterized by a senior labmate, Yuewang Huang.

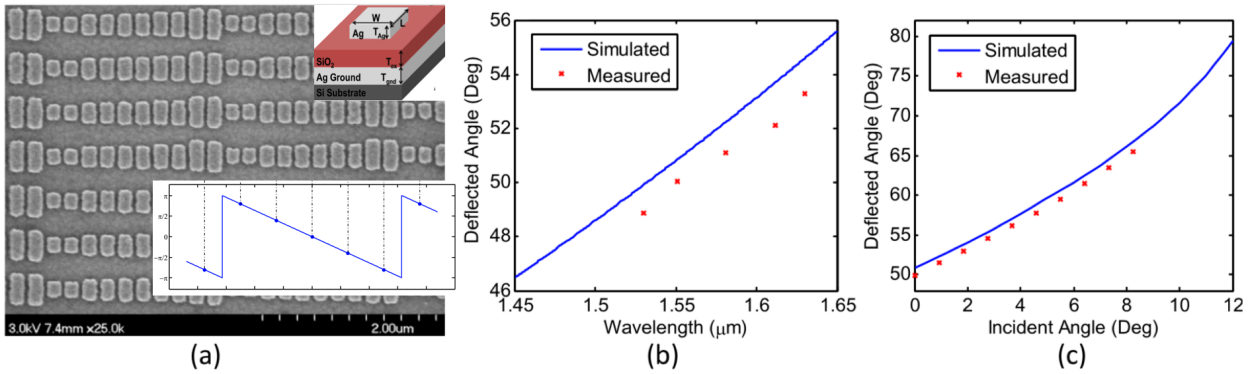

Figure 4.3: (a) SEM image of the fabricated grating. (Inset 1) The 2π phase variation of one supercell that includes 10 unit cells with 160nm widths and varying lengths (170nm-350nm) separated by 40nm. (Inset 2) 3D structure of single unit cell (200nm x 500nm) with 30nm, 50nm and 200nm thicknesses from top to bottom. (b) Simulated and measured deflected angle for different wavelengths at normal incidence. (c) Simulated and measured deflected angle for different incident angles at 1550 nm. Reproduced from [Huang et. al., Appl. Phys. Lett., 104(16):161106 (2014) [66]], with the permission of AIP Publishing.

Even though this is a planar structure, it is working as a blazed grating thanks to wavefront engineering. Figure 4.3a shows the SEM image of the fabricated device, 3D structure of the unit cell and the super cell that achieves 2π phase variation. The wavefront manipulating capability of this planar grating originates from plasmonic resonance in the metallic structures that act as an electric dipole scattering with a phase delay controlled by its dimension. Single layer metasurfaces limit the wavefront manipulation to π due to the single dipole nature of the resonance [67, 68]. By inserting a ground plane under patterned metasurfaces to form the metal-insulator-metal (MIM) structure, additional dipole oscillations can be excited due to the coupling between metal surfaces that can increase phase variation up to 2π [69, 70]. Higher power efficiency is also expected from high reflection by the ground plane. As the metal and dielectric, silver (Ag) and silicon dioxide (SiO_2) are chosen due to the transparency of SiO_2 and the fact that Ag has four times lower damping compared to gold in the telecommunication window [71, 72]. The power efficiency of the grating at 1550nm was measured to be as high as 75.6% for TE polarized waves at normal incidence [66]. For more details in the design, fabrication and characterization processes of this planar blazed grating along with the theory on how to achieve wavefront engineering, you can check Mr.

Huang's dissertation [73].

In the laser scanning system, we are mainly interested in the grating efficiency and the dispersion power. Figure 4.3b shows simulated and measured deflected angles for different wavelengths at normal incidence. Since, the configuration is similar to Figure 4.2d, the measured angles are twice more than the blaze angle ($\theta_m = 2\gamma$) for given wavelength. Therefore, this measurement also demonstrates the dispersion of the grating as $\sim 0.4^o/10$nm that is the slope of the curve. On the other hand, Figure 4.3c is showing the variation of the deflected angle for different incident angles at 1550 nm. Even though the power efficiency of the grating is decreasing with increasing oblique incidence, the grating works linearly up to 8^o. The slope of 2 shows that deflected angles follow the specular reflection.

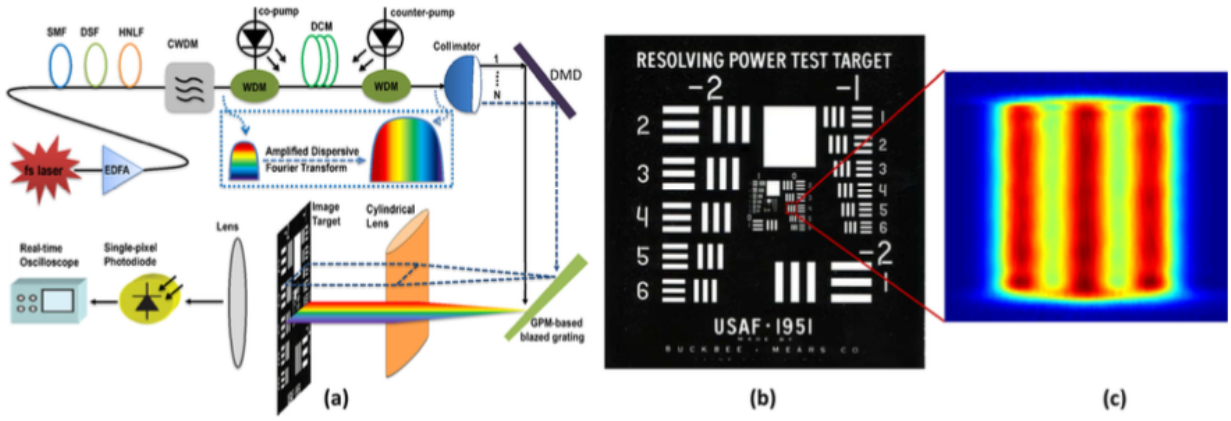

Figure 4.4: (a) The setup of the imaging system using the fabricated GPM-based blazed grating. (b) The whole pattern of 1951 USAF test chart. (c) The recovered image of the area enclosed by the red dashed box in (b) (Element 4 of Group 0 in 1951 USAF). A resolution <300 μm can be achieved. Reproduced from [Huang et. al., Appl. Phys. Lett., 104(16):161106 (2014) [66]], with the permission of AIP Publishing.

This GPM-based blazed grating is employed in the real time dispersive laser scanner system to improve the power efficiency as shown in Figure 4.4a. With this system, a portion of 1951 USAF resolution test chart (Figure 4.4b) is scanned. The captured time domain signals are post-processed in MATLAB and plotted to generate 2D scan results. Figure 4.4c shows the recovered image of Element 4 of Group 0 that is enclosed in red box. The width and spacing of vertical lines are 353.55μm.The results show that the resolution is better than 300μm.

However, this measurement does not show the true resolution capability of this grating, because small footprint of the fabricated structure limits the beam size (d), therefore resolution (Δx). As given in Eq. 3.1c, lateral resolution of the system is inversely proportional to the beam size due to the diffraction limit.

4.3 Scanning Speed Improvement

As it is discussed in Chapter 3, the lateral scanning speed is determined by the repetition rate of the MLL (20MHz) and vertical scanning speed is limited by the DMD's scan rate (5kHz). It is clearly seen that, DMD is the main limiting factor for the speed of the system. The current system is scanning same area, hence capturing same waveform for 4000 consecutive pulses. Even though, this situation can be utilized to improve SNR of the system via signal averaging, it is better to increase the scanning speed of the system. Since speed scaling is not straightforward and requires extra components, there will still be plenty of signals for averaging after scaling.

One approach is mentioned earlier in Chapter 4.1 by facilitating a fast pulse picker device such as acousto-optic deflector and utilize several DMDs. In this way, even though vertical scan speed of single DMD is not improved, total scan speed of the system is scaled up by the amount of parallelism (N), because wider area scanned at the same time. For such system, there will be a group of data consisting of N consecutive time signals which represent N different area scans. Still, this group of N measurements are repeating itself until DMDs refresh their pattern.

Here, I will discuss how the vertical scan rate of single DMD can be effectively increased. Single DMD will be facilitated as two DMDs with keeping two strips of the DMD ON and sending two pulses that are delayed in time and separated in space. The idea is similar to

the parallelization of DMDs, however the complexity of adding all the controls of each DMD and synchronization of them are removed. Only the DMD patterns that are shown in Figure 3.7 will be edited as in Figure 4.5. The NxM strips turned on at the same time are color coded and two beams hitting on the DMD are shown. The separation of the beams in the space should be 4.15mm that is half of the DMD height.

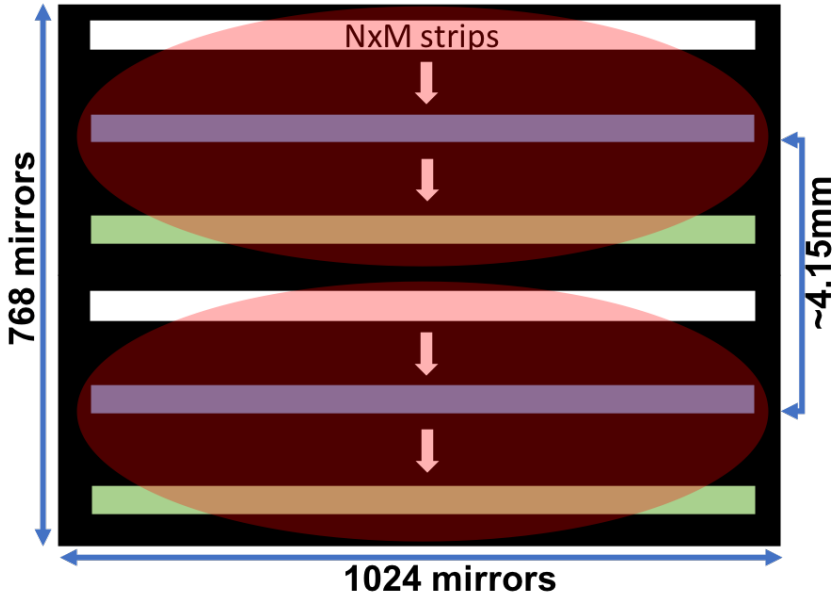

Figure 4.5: Modified DMD pattern to effectively increase vertical scan rate. Color coded NxM strips show the micromirrors that are ON at the same time. Red transparent ellipses show two beams that are separated in time and space for 25ns and ∼4.15mm respectively.

Also, the beams should be 25ns apart from each other in time. This idea of speed improvement is applicable to our laser scanner, since the time axis is not fully utilized. The femtosecond pulses with 20MHz repetition rate are broadened up to 13.5ns, since 20nm bandwidth is employed after SC generation and -675ps/nm dispersion is used in amplified DFT setup. Since period of MLL pulses are 50ns, we are utilizing only 27% of the time domain. Therefore up to 4 times speed increase is possible, if one would like to utilize 100% of the time. In order to utilize the time, the pulses after the amplified dispersive fourier transform are split into two through fiber optic 50/50 beam splitter and one arm is delayed for ∼25ns through ∼5m long single mode fiber as shown in Figure 4.6. The two beams

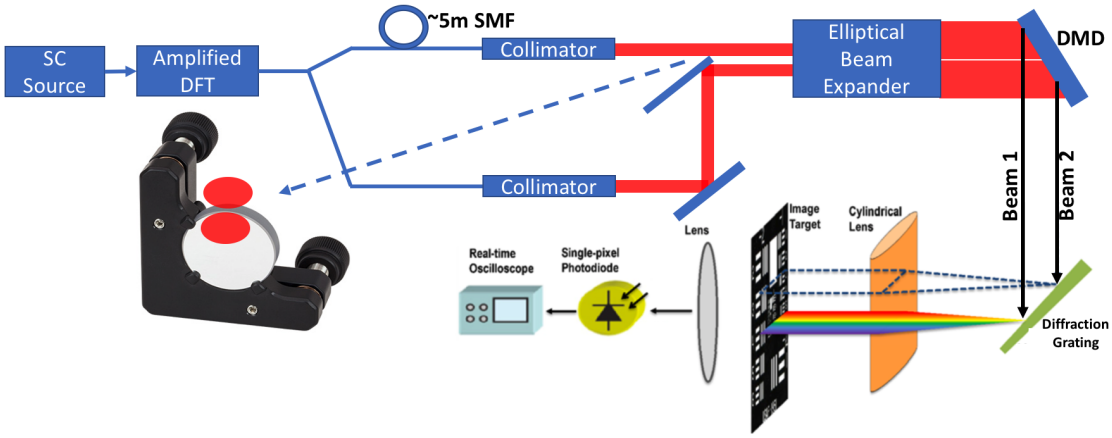

Figure 4.6: Modified laser scanner setup for two beam scanning. Inset shows the spatial position of two beams on the plane of second mirror used in alignment.

after the delay is shown in Figure 4.7. It is clearly seen that, 13.5ns pulses are delayed for ∼25ns and there is still more to be utilized. Later the two beams are transmitted to free space via collimators, expanded and shot on the DMD with ∼4.15mm separation. In order to align two beams and bring them close to each other, I used two mirror alignment where one mirror is mounted on a clear edge mirror mount in order to eliminate obstacles for other beam as shown in Figure 4.6. Elliptical beam expander is using cylindrical lenses to generate 11mmx4mm elliptical beams.

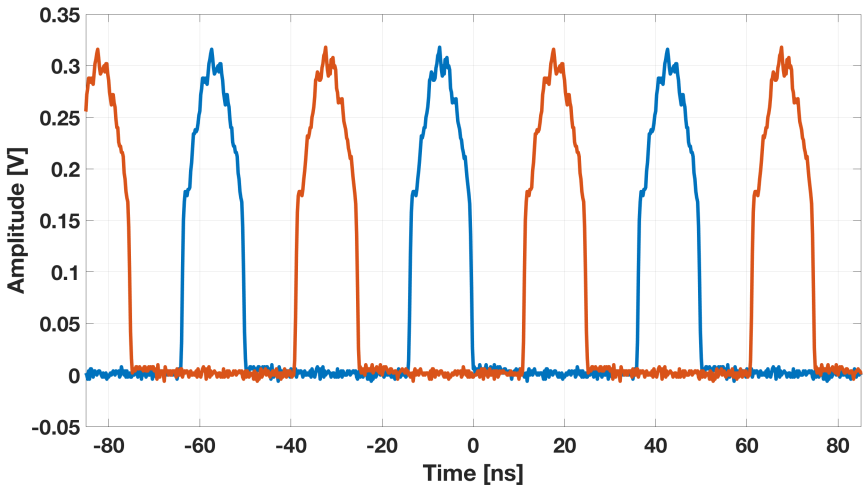

Figure 4.7: Splitted and Time Delayed Envelopes that are ∼13.5ns wide and ∼25ns apart from each other.

The same delay can be achieved in free space with using free space beam splitters, however the required propagation distance will be 7.5m, therefore 3.75m optical path difference is required due to double pass. Beam divergence will be the main limitation of free space systems. On the other hand, it is easier to add small translation by facilitating corner cubes, therefore if further speed improvement is desired (e.g. 4 times), corner cubes can be better option. It is also possible to utilize both systems together with inserting time delay in fiber and achieving spatial translation in free space with corner cubes. Such system will have fine control of time delay and spatial translation with the cost of extra 3dB loss, since free space beam splitter will still be required.

Chapter 5

Conclusion

In this thesis, scalable dispersive laser scanner system and ideas on how to improve the 2D scan area, power efficiency and scan speed of the system are investigated.

The proposed fast dispersive laser scanning system uses the space wavelength mapping for the lateral scanning and digital micro mirror arrays for vertical scanning to achieve real-time 2D scanning. By dynamically switching the states of the micro mirrors, the position of the spatially dispersed beam is moved over the target. In the experiments, $\sim$20mm^2 wide area with $\sim$150μm lateral and $\sim$160μm vertical resolution is monitored for the proof of concept. By facilitating state of the art DMDs, MEMS based amplified time stretched system can achieve fast vertical scanning with frame rates up to 32.5kHz and with resolution down to single mirror pitch size of 10.8μm. Since, single mirror pitch size of 10.8μm resolution is not achievable with the current system due to power limitations, the ideas to improve power efficiency of the system is investigated. A GPM based blazed grating with 75.6% efficiency at 1550nm that is designed and fabricated by another senior labmate is employed in the system. Additionally, to increase the scanned area and vertical scan speed, parallelization ideas and two beam scanning systems are presented.

Bibliography

[1] W. Caputi. Stretch: A time-transformation technique. *IEEE Transactions on Aerospace and Electronic Systems*, AES-7(2):269–278, March 1971.

[2] S. K. Kalyoncu, Y. Huang, Q. Song, and O. Boyraz. Analytical study on arbitrary waveform generation by MEMS micro mirror arrays. *Optics Express*, 20(25):27542–27553, 2012.

[3] J. Azana, L. R. Chen, M. A. Muriel, and P. W. E. Smith. Experimental demonstration of real-time Fourier transformation using linearly chirped fiber bragg gratings. *Electronic Letters*, 35:2223–2224, 1999.

[4] K. Goda, A. Mahjoubfar, C. Wang, A. Fard, J. Adam, D. R. Gossett, A. Ayazi, E. Sollier, O. Malik, E. Chen, et al. Hybrid dispersion laser scanner. *Scientific reports*, 2, 2012.

[5] F. Coppinger, A. S. Bhushan, and B. Jalali. Time magnification of electrical signals using chirped optical pulses. *Electronic Letters*, 34(4):399–400, February 1998.

[6] A. S. Bhushan, F. Coppinger, and B. Jalali. Time stretched analogue-to-digital conversion. *Electronic Letters*, 34(9):839–840, April 1998.

[7] F. Coppinger, A. S. Bhushan, and B. Jalali. Photonic time stretch and its application to analog-to-digital conversion. *IEEE Transactions on Microwave Theory and Techniques*, 47(7):1309–1314, 1999.

[8] S. K. Kalyoncu, R. Torun, Y. Huang, Q. Zhao, and O. Boyraz. Fast dispersive laser scanner by using digital micro mirror arrays. *ASME Journal of Micro- and Nano-Manufacturing*, 2:021004–1–021004–6, June 2014.

[9] K. Goda, K. Tsia, and B. Jalali. An ultrafast barcode reader using amplified dispersive Fourier transform. In *LEOS 2008 - 21st Annual Meeting of the IEEE Lasers and Electro-Optics Society*, pages 644–645. IEEE Lasers and Electro-Optics Society 2008, 9-13 November 2008 2008.

[10] S. P. Singh and N. Singh. Nonlinear effects in optical fibers: Origin, management and applications. *Progress In Electromagnetics Research*, 73:249–275, 2007.

[11] G. P. Agrawal. *Nonlinear Fiber Optics*. Academic Press, US, 3 edition, 2009.

[12] O. Boyraz. 285A lecture slides 3, 2014. [Online; accessed 10-June-2014].

[13] G. P. Agrawal. *Fiber-Optic Communication Systems*. John Wiley & Sons, 3 edition, 2002.

[14] M. N. Islam, L. F. Mollenauer, and R. H. Stolen. Cross-phase modulation in optical fibers. *Optics Letters*, 12(8), 1987.

[15] B. Washburn. Numerical solutions to nonlinear schrodinger equation. [Online; accessed 10-June-2014].

[16] S. K. Kalyoncu. *Raman Based Dispersive Systems for Short Pulse Generation and Optical Signal Processing*. PhD thesis, University of California, Irvine, 2013.

[17] Corning. Corning smf-28 optical fiber product information, 2002. [Online; accessed 10-Nov-2018].

[18] RP Photonics Encyclopedia. Erbium-doped gain media. [Online; accessed 10-June-2014].

[19] H. Rong, S. Xu, O. Cohen, O. Raday, M. Lee, V. Sih, and M. Paniccia. A cascaded silicon Raman laser. *Nature photonics*, 2(3):170–174, 2008.

[20] R. H. Stolen. Fundamentals of raman amplification in fibers. In M. N. Islam, editor, *Raman amplifiers for telecommunications*, volume 1, chapter 2. Springer, 2004.

[21] C. V. Raman. A new radiation. *Indian Journal of physics*, 2:387–398, 1928.

[22] H. A. Haus and M. Nakazawa. Theory of the fiber raman soliton laser. *JOSA B*, 4(5):652–660, 1987.

[23] J. Bromage. Raman amplification for fiber communications systems. *Journal of Lightwave Technology*, 22(1):79, 2004.

[24] J. Chou, O. Boyraz, D. Solli, and B. Jalali. Femtosecond real-time single-shot digitizer. *Applied Physics Letters*, 91(16):161105–161105, 2007.

[25] S. K. Kalyoncu, Y. Huang, E. K. Tien, E. Adas, D. Yildirim, and O. Boyraz. Noise performance of time stretch system with distributed and discrete amplifiers. In *CLEO: Science and Innovations*, page CTuA7. Optical Society of America, 2011.

[26] Tech-Etch. Photoetched fuel cell plates, frames, support screens & end caps. [Online; accessed 10-June-2014].

[27] International Partnership for Hydrogen and Fuel Cells in the Economy. The role of battery electric vehicles, plug-in hybrids and fuel cell electric vehicles. [Online; accessed 10-June-2014].

[28] G. Wilkening and H. Bosse. Nano- and micrometrology state-of-the-art and future challenges. *MAPAN-Journal of Metrology Society of India*, 20(2):125–151, 2005.

[29] H. N. Hansen, G. Tosello, S. Gasparin, and L. De Chiffre. Dimensional metrology for process and part quality control in micro manufacturing. *International Journal of Precision Technology*, 2(2):118–135, 2011.

[30] H. U. Danzebrink, L. Koenders, G. Wilkening, A. Yacoot, and H. Kunzmann. Advances in scanning force microscopy for dimensional metrology. *CIRP Annals-Manufacturing Technology*, 55(2):841–878, 2006.

[31] J. C. Wyant. White light extended source shearing interferometer. *Applied Optics*, 13(1):200–202, 1974.

[32] M. Minsky. Memoir on inventing the confocal scanning microscope. *Scanning*, 10(4):128–138, 1988.

[33] G. F. Marshall and G. E. Stutz. *Handbook of optical and laser scanning*. CRC Press, 2004.

[34] T. Fujii and T. Fukuchi. *Laser remote sensing*. CRC Press, 2005.

[35] C. Dotson, R. Harlow, and R. L. Thompson. *Fundamentals of dimensional metrology*. Thomson Learning, 2003.

[36] C. Weitkamp. *Range-resolved optical remote sensing of the Atmosphere*. Springer, 2005.

[37] B. Schwarz. Mapping the world in 3d. *Nat. Photonics*, 4(7):429–430, 2010.

[38] A. Sinha. *Vibration of mechanical systems*. Cambridge University Press, 2010.

[39] W. Osten. *Optical inspection of microsystems*. CRC Press, 2006.

[40] J. A. Pelesko and D. H. Bernstein. *Modeling Mems and Nems*. CRC press, 2002.

[41] G. Popescu, T. Ikeda, K. Goda, C. A. Best-Popescu, M. Laposata, S. Manley, R. R. Dasari, K. Badizadegan, and M. S. Feld. Optical measurement of cell membrane tension. *Physical review letters*, 97(21):218101, 2006.

[42] W. Göbel, B. M. Kampa, and F. Helmchen. Imaging cellular network dynamics in three dimensions using fast 3d laser scanning. *Nature methods*, 4(1):73–79, 2006.

[43] J. B. Pawley. *Handbook of biological confocal microscopy*. Plenum Press, 1995.

[44] W. Denk, J. H. Strickler, W. W. Webb, et al. Two-photon laser scanning fluorescence microscopy. *Science*, 248(4951):73–76, 1990.

[45] A. Hoffman, M. Goetz, M. Vieth, P. R. Galle, M. F. Neurath, and R. Kiesslich. Confocal laser endomicroscopy: technical status and current indications. *Endoscopy*, 38(12):1275–1283, 2006.

[46] A. Tárnok and A. O. H. Gerstner. Clinical applications of laser scanning cytometry. *Cytometry*, 50(3):133–143, 2002.

[47] R. Conant. *Micromachined mirrors*, volume 12. Springer, 2002.

[48] Z. Yaqoob and N. A. Riza. Passive optics no-moving-parts barcode scanners. *Photonics Technology Letters, IEEE*, 16(3):954–956, 2004.

[49] D. R. Pape, A. P. Goutzoulis, and S. V. Kulakov. *Design and fabrication of acousto-optic devices*. M. Dekker, 1994.

[50] I. W. Jung, J. Wang, and O. Solgaard. Optical pattern generation using a spatial light modulator for maskless lithography. *Selected Topics in Quantum Electronics, IEEE Journal of*, 13(2):147–154, 2007.

[51] D. Dudley, W. M. Duncan, and J. Slaughter. Emerging digital micromirror device (dmd) applications. In *Micromachining and Microfabrication*, pages 14–25. International Society for Optics and Photonics, 2003.

[52] S. K. Nayar, V. Branzoi, and T. E. Boult. Programmable imaging using a digital micromirror array. In *Computer Vision and Pattern Recognition, 2004. CVPR 2004. Proceedings of the 2004 IEEE Computer Society Conference on*, volume 1, pages I–436. IEEE, 2004.

[53] DLP Texas Instruments. Dlp 0.55xga chipset, 2010. [Online; accessed 10-May-2013].

[54] R. S. Nesbitt, S. L. Smith, R. A. Molnar, and S. A. Benton. Holographic recording using a digital micromirror device. In *Electronic Imaging'99*, pages 12–20. International Society for Optics and Photonics, 1999.

[55] L. J. Hornbeck et al. Digital light processing for high-brightness, high-resolution applications. In *Proc. SPIE*, volume 3013, pages 27–40, 1997.

[56] DLP Texas Instruments. Mems dlp technology - getting started, 2010. [Online; accessed 10-May-2013].

[57] DLP Texas Instruments. Application report: Dmd 101: Introduction to digital micromirror device (dmd) technology, 2008. [Online; accessed 10-May-2013].

[58] DLP Texas Instruments. Application report: Dlp system optics, 2010. [Online; accessed 10-May-2013].

[59] DLP Texas Instruments and ASME. The digital micromirror device: A historic mechanical engineering landmark, 2008. [Online; accessed 10-May-2013].

[60] O. Boyraz, J. Kim, M. N. Islam, E. Coppinger, and B. Jalali. 10 Gb/s multiple wavelength, coherent short pulse source based on spectral carving of supercontinuum generated in fibers. *Lightwave Technology, Journal of*, 18(12):2167–2175, 2000.

[61] S. K. Kalyoncu, Y. Huang, Q. Song, and O. Boyraz. Fast arbitrary waveform generation by using digital micromirror arrays. *Photonics Journal, IEEE*, 5(1):5500207–5500207, 2013.

[62] S. K. Kalyoncu, Y. Huang, R. Torun, Q. Zhao, and O. Boyraz. Fast dispersive laser scanner by using digital micro mirror arrays. In *CLEO: Applications and Technology*, pages JTu4A–30. Optical Society of America, 2013.

[63] DLP Texas Instruments. Digital exposure, 2010. [Online; accessed 10-May-2013].

[64] A. Yariv and P. Yeh. *Photonics: Optical Electronics in Modern Communications*. Oxford University Press, Oxford, 6 edition, 2007.

[65] ThorLabs. Diffraction gratings tutorial, 2018. [Online; accessed 10-Nov-2018].

[66] Y. Huang, Q. Zhao, S. K. Kalyoncu, R. Torun, Y. Lu, and F. CapolinoO. Boyraz. Phase-gradient gap-plasmon metasurface based blazed grating for real time dispersive imaging. *Applied Physics Letters*, 104(16):161106, 2014.

[67] R. Blanchard, G. Aoust, P. Genevet, N. Yu, M. A. Kats, Z. Gaburro, and F. Capasso. Modeling nanoscale v-shaped antennas for the design of optical phased arrays. *Physical Review B*, 85(15):155457, 2012.

[68] A. Pors and S. I. Bozhevolnyi. Plasmonic metasurfaces for efficient phase control in reflection. *Optics Express*, 21(22):27438–27451, 2013.

[69] S. Sun, Q. He, S. Xiao, Q. Xu, X. Li, and L. Zhou. Gradient-index meta-surfaces as a bridge linking propagating waves and surface waves. *Nature Materials*, 11(5):426, 2012.

[70] S. Sun, K. Yang, C. Wang, T. Juan, W. T. Chen, C. Y. Liao, Q. He, S. Xiao, W. Kung, G. Guo, et al. High-efficiency broadband anomalous reflection by gradient meta-surfaces. *Nano Letters*, 12(12):6223–6229, 2012.

[71] P. B. Johnson and R. W. Christy. Optical constants of the noble metals. *Physical Review B*, 6(12):4370, 1972.

[72] P. R. West, S. Ishii, G. V. Naik, N. K. Emani, V. M. Shalaev, and A. Boltasseva. Searching for better plasmonic materials. *Laser & Photonics Reviews*, 4(6):795–808, 2010.

[73] Y. Huang. *Integrated Optical Signal Processing Based on Optical Waveguides and Wavefront-engineered Planar Devices*. PhD thesis, University of California, Irvine, 2014.